A TBX5-dependent compartment boundary patterns the cardiac interventricular septum

Irfan S. Kathiriya[1,#], Martin H. Dominguez[2,3], Kavitha S. Rao[1,2], Jonathon M. Muncie-Vasic[2], W. Patrick Devine[2,4], Kevin M. Hu[1,2], Swetansu K. Hota[2], Bayardo I. Garay[1], Diego Quintero[2], Piyush Goyal[1,2], Megan N. Matthews[1], Reuben Thomas[2], Tatyana Sukonnik[2], Dario Miguel-Perez[2], Sarah Winchester[2], Emily F. Brower[2], André Forjaz[5], Pei-Hsun Wu[5], Denis Wirtz[5], Ashley L. Kiemen[5], Benoit G. Bruneau[2,6,7,8,#]

[#]corresponding authors

[1] Department of Anesthesia and Perioperative Care, University of California, San Francisco, San Francisco, CA

[2] Gladstone Institutes, San Francisco, CA

[3] Department of Medicine, University of California, San Francisco, San Francisco, CA

[4] Department of Pathology, University of California, San Francisco, San Francisco, CA

[5] Department of Chemical and Biomolecular Engineering, Johns Hopkins University, Baltimore, MD

[6] Roddenberry Center for Stem Cell Biology and Medicine, Gladstone Institutes, San Francisco, CA

[7] Cardiovascular Research Institute, University of California, San Francisco, San Francisco, CA

[8] Department of Pediatrics, University of California, San Francisco, San Francisco, CA

Abstract. (147 words).

Failure of septation of the interventricular septum (IVS) is the most common congenital heart defect (CHD), but mechanisms for patterning the IVS are largely unknown. We show that a *Tbx5*$^{+}$/*Mef2cAHF*$^{+}$ progenitor lineage forms a compartment boundary bisecting the IVS. This coordinated population originates at a first- and second heart field interface, subsequently forming

a morphogenetic nexus. Ablation of *Tbx5*$^{+}$/*Mef2cAHF*$^{+}$ progenitors cause IVS disorganization, right ventricular hypoplasia, and mixing of IVS lineages. Reduced dosage of the CHD transcription factor TBX5 disrupts boundary position and integrity, resulting in ventricular septation defects (VSDs) and patterning defects including *Slit2* and *Ntn1* misexpression. Reducing NTN1 dosage partly rescues cardiac defects in *Tbx5* mutant embryos. Loss of *Slit2* or *Ntn1* causes VSDs and perturbed septal lineage distributions. Thus, we identify essential cues that direct progenitors to pattern a compartment boundary for proper cardiac septation, revealing new mechanisms for cardiac birth defects.

Main.

Alterations to the orchestrated patterning of heart development can lead to CHDs. CHDs are the most common birth defects and are a leading non-infectious cause of death in the first year of life. Nearly half of patients with CHDs have ventricular septal defects (VSDs) or atrial septal defects (ASDs), in isolation or in combination with other anatomic defects, including abnormal chamber formation. For example, atrioventricular canal (AVC) defects include VSDs, ASDs and abnormal development of the atrioventricular (AV) valves, with severe cases leading to chamber hypoplasia and functional single ventricle physiology. There is a large gap in our understanding of how early developmental events pattern cardiac morphogenesis and anatomy. Addressing this understudied need can inform diagnostic prognosis, family planning and therapeutic approaches for CHDs.

Complete atrioventricular septation into four chambers allows for separation of systemic and pulmonary circulations and enables higher levels of oxygen for transport in arterial blood. Some progress has been made to determine the embryology of the primordium for the ventricular septum.[1,23] A dye-labelled approach in chick embryos revealed that labelling of the ventral surface of the linear heart tube becomes positioned at the outer curvature of the linear heart tube [1,2]. When labelled at the outer curvature upon rightward looping, the label was found at the apical

border of the primary interventricular foramen [1,2]. Discovery of the *Ganglion Nodosum* epitope from chick, which demarcated the primary interventricular foramen and subsequently the IVS, AV junction and ventricular conduction system in mouse, chick and humans, led to the description of a "primary ring" for the ventricular septum [3–5].

Discrete early cardiac progenitors in mesoderm contribute to specific cardiac anatomy [6–8]. The first heart field (FHF) gives rise primarily to the left ventricle (LV) and parts of the atria, while the second heart field (SHF) contributes predominantly to the right ventricle (RV), outflow tract (OFT) and portions of the atria [9]. The heart fields can be largely recapitulated by marking lineage-labelled progenitors at gastrulation. Specifically, a lineage labelled by the CHD-linked transcription factor *Tbx5* (*Tbx5*$^+$-lineage) contributes to the LV and atria, while the anterior heart field enhancer of *Mef2c* (*Mef2cAHF*$^+$)-lineage largely contributes to the RV and OFT [6].

Both the LV and RV lineages supply descendants to the interventricular septum (IVS) and establish a mutual border between the two lineages [6,10]. Clonal analysis shows segregation at the IVS of the two lineages into non-intermingling cellular compartments, on either the left or right sides of the IVS [6,10]. This lineage configuration is reminiscent of a compartment boundary in *Drosophila* wing imaginal disc or at the vertebrate midbrain-hindbrain boundary [11–13]. Using an intersectional-lineage labelling approach, a subset of cardiac progenitor cells labeled by both *Tbx5*$^+$*/Mef2cAHF*$^+$ were described with contributions to the left side of this apparent compartment boundary [6]. Understanding the role of the *Tbx5*$^+$*/Mef2cAHF*$^+$ lineage-labeled compartment boundary at the IVS may reveal clues about IVS patterning with potential relevance for VSD etiologies. More broadly, how disturbances to compartment boundaries contribute to birth defects is largely unknown.

Here, we combined genetic lineage labeling with light sheet microscopy to follow contributions of *Tbx5*$^+$*/Mef2cAHF*$^+$ precursors to a compartment boundary during cardiac morphogenesis. We ablated *Tbx5*$^+$*/Mef2cAHF*$^+$ precursors to determine the essential roles of the lineage-labeled compartment boundary for cardiac septation and chamber development. We

leveraged a genetic lesion of the CHD gene *Tbx5* to uncover the genetic regulation of the *Tbx5*$^{+}$/*Mef2cAHF*$^{+}$ lineage-labeled compartment boundary for proper IVS formation. We deployed single cell RNA sequencing (scRNAseq) to discover novel Tbx5-sensitive cues that are essential for compartment boundary regulation of IVS patterning during heart development.

Results.

<u>Early cardiac progenitors for the IVS, IAS and AVC.</u> We used conditional dual lineage labelling by *Tbx5*$^{CreERT2/+}$ or *Mef2cAHF-DreERT2* and marked cells during gastrulation at embryonic day (E)6.5 by tamoxifen-induced recombination. We followed reporter-labeled lineages by epifluorescence microscopy, histology or light sheet microscopy (Figure 1). At E14.5, the *Tbx5*$^{+}$ lineage contributed to the left side of the IVS, often ending at a presumptive line marked at the apex by the IV groove, consistent with previous reports suggesting a lineage boundary [6,10]. *Tbx5*$^{+}$ and *Mef2cAHF*$^{+}$ lineages showed largely complementary patterns, with notable overlap of *Tbx5*$^{+}$ and *Mef2cAHF*$^{+}$ lineages at the IVS, AVC and IAS (Figure 1B, D, F). To better visualize the *Tbx5*$^{+}$/*Mef2cAHF*$^{+}$ lineage, we used a conditional intersectional-lineage labeling approach. Using lineage reporters responsive to both CreERT2 and DreERT2 [14], we observed a striking spatial pattern of the *Tbx5*$^{+}$/*Mef2cAHF*$^{+}$ lineage in the IVS, AVC and IAS. At E14.5, the septal lineage extended to the apex of the heart via the IVS, to the base of the heart at the AV canal, as well as to the IAS superiorly[15–18] (Figure 1H-J). These results expanded upon previous findings in the developing IVS at E10.5 [6], by identifying contributions from *Tbx5*$^{+}$/*Mef2cAHF*$^{+}$ progenitors to additional anatomic sites during chamber formation and septation. Moreover, we deduced that lineage contributions to sites of cardiac septation were derived from *Tbx5*$^{+}$/*Mef2cAHF*$^{+}$ progenitors at E6.5 (Supp. Figure 1), but not later at E8.5 or E10.5, implicating a narrow, early window for capturing *Tbx5*$^{+}$/*Mef2cAHF*$^{+}$ septal progenitors during cardiac mesoderm formation.

Tbx5^{+}*/Mef2cAHF*$^{+}$ septal lineage is prefigured in early mouse heart development. To assess the lineage derived from *Tbx5*$^{+}$*/Mef2cAHF*$^{+}$-septal progenitors during early heart development, we examined the localization of the lineage prior to heart tube formation at E8.0 (Figure 2). By light sheet imaging, the pattern of the *Tbx5*$^{+}$*/Mef2cAHF*$^{+}$ lineage was detected at the dorsal aspect of the *Tbx5*$^{+}$ lineage, at an interface between the presumptive first and second heart fields (Figure 2A-E"). Cell segmentation at this early stage revealed that the *Tbx5*$^{+}$*/Mef2cAHF*$^{+}$ lineage resembled a nascent halo of cells that became readily apparent at later stages of heart development (Figure 2F-I).

We further examined the lineage contributions of *Tbx5*$^{+}$*/Mef2cAHF*$^{+}$ septal progenitors at subsequent timepoints during cardiac morphogenesis. By light sheet microscopy at the linear heart tube stage at E8.25, the labeled *Tbx5*$^{+}$*/Mef2cAHF*$^{+}$ lineage appeared intricately arranged into a ring of cells between the future left and right ventricles (Figure 2J, K). This circlet configuration was maintained during rightward looping of the heart at E8.5 (Figure 2O-Q) and subsequent chamber formation. At E10.5, we observed a band of lineage-labeled cells from the interventricular groove at the outer curvature to the inner curvature near the AV groove that extended posteriorly to the atria (Figure 2R-T), reminiscent of the "primary ring" [3–5]. Optical sections showed the labeled lineage superiorly at a crossroads of the AVC, outflow tract and atria (Figure 2S). This populates a morphogenetic nexus where VSDs can occur due to abnormal connections between the IVS and the AV cushions, outflow tract cushions, or the muscular septum itself. In the atria, we noted lineage-labeled cells at the midline, superiorly and inferiorly, suggesting that the Tbx5^{+}/Mef2cAHF^{+} lineage potentially mark the presumptive location of the IAS for later stages (Supp. Figure 2B-E). Consequently, this data is consistent with a notion that the *Tbx5*$^{+}$*/Mef2cAHF*$^{+}$ lineage is configured early in heart development, well before subsequent morphogenetic events such as chamber formation and cardiac septation.

129 IVS disorganization and ventricular hypoplasia from cell ablation of Tbx5^{+}/Mef2cAHF^{+}
130 progenitors. To determine a role for the *Tbx5^{+}/Mef2cAHF^{+}* septal progenitors, we conditionally
131 ablated these cells at E6.5, then evaluated heart development. We generated an intersectional
132 recombinase-responsive *DTA176* transgenic mouse line at the *Hip11* safe harbor locus, by which
133 cells would be killed where approximately 100-200 molecules of DTA176 were expressed [15]. Upon
134 tamoxifen administration to pregnant dams at E6.5, intersectional-*DTA* mutant (*Tbx5$^{CreERT2/+}$;*
135 *Mef2cAHF-DreERT2; Hip11$^{Intersectional\text{-}DTA176/+}$*) embryos at E9.5 displayed RV hypoplasia (Figure
136 3A, B). At E12.5, RV hypoplasia persisted (Figure 3C-J), and the IVS was disorganized and non-
137 compacted at a blunted IV groove (Figure 3H, J). Further, there were defects of the AV cushions
138 and absence of the IAS (Figure 3H, J). A few *Tbx5^{+}/Mef2cAHF^{+}* lineage cells remained in mutant
139 embryos, likely reflecting some degree of inefficient dual recombination of both the reporter allele
140 and the intersectional-*DTA* transgene. Beyond E12.5, intersectional-*DTA* mutant embryos were
141 not recovered. Hence, these findings suggested that the *Tbx5^{+}/Mef2cAHF^{+}* septal progenitors
142 were not only important for IVS development and AV septation, but also for RV chamber
143 formation.
144
145 Lineage mixing from disruption of an IVS compartment boundary upon ablation of
146 *Tbx5^{+}/Mef2cAHF^{+}* septal progenitors. We hypothesized that the *Tbx5^{+}/Mef2cAHF^{+}* septal
147 progenitors establish a compartment boundary at the IVS. Upon ablation of *Tbx5^{+}/Mef2cAHF^{+}*
148 septal progenitors, we predicted that if either lineage expanded into the other ventricular chamber,
149 then this would suggest lineage mixing from loss of compartment boundary integrity. To determine
150 if *Tbx5^{+}/Mef2cAHF^{+}* septal progenitors were essential for a compartment boundary at the IVS, we
151 tested the effects of ablating *Tbx5^{+}/Mef2cAHF^{+}* septal progenitors on lineage segregation. We
152 quantified the distributions of the *Mef2cAHF^{+}* or *Tbx5^{+}* lineages at E10.5 after tamoxifen
153 administration at E6.5, by quantifying fluorescence intensity as a linear profile across the
154 ventricular chambers by light sheet microscopy. In control (*Tbx5$^{CreERT2/+}$;Mef2cAHF-*

155 *DreERT2;Hip11*$^{+/+}$) (n=2) embryos at E10.5, cells of the *Mef2cAHF*$^{+}$ lineage were enriched in the
156 RV. Cells of the *Tbx5*$^{+}$ lineage were highly enriched in the LV and rarely found in the RV, and
157 both lineages overlapped at the developing IVS. This data was consistent with observations of
158 lineage segregation at the IVS during later stages of heart development. However, in mutant
159 intersectional-*DTA* (*Tbx5*$^{CreERT2/+}$*;Mef2cAHF-DreERT2;Hip11*$^{Intersectional\text{-}DTA176/+}$) (n=2) embryos at
160 E10.5, cells of the *Mef2cAHF*$^{+}$ lineage were less leftward in the corresponding region of targeted
161 cell ablation, suggesting a rightward retreat of the Mef2cAHF^{+} lineage from ablation of
162 *Tbx5*$^{+}$*/Mef2cAHF*$^{+}$ progenitors. In contrast, cells of the Tbx5^{+} lineage in intersectional-*DTA*
163 mutants were observed more rightward, including in the RV. Therefore, we inferred that
164 *Tbx5*$^{+}$*/Mef2cAHF*$^{+}$ progenitors were essential for preventing lineage mixing between the RV and
165 LV, by maintaining compartment boundary integrity at the developing IVS.
166
167 <u>Heterozygous loss of *Tbx5* in the IVS leads to VSDs</u>. *TBX5* is a transcription factor gene that
168 causes VSDs in Holt-Oram Syndrome from haploinsufficiency in humans [16–18] and mice [19]. We
169 wondered if heterozygous loss of *Tbx5* in the IVS alone would cause VSDs. We used the
170 *Mef2cAHF-Cre* [20] in combination with a conditional deletion of *Tbx5* (*Tbx5*^{flox}) [19], to conditionally
171 delete *Tbx5* heterozygously in a domain that overlaps with *Tbx5* expression at the IVS [21]. We
172 observed membranous VSDs in *Mef2cAHF-Cre*;*ROSA26*$^{mTmG/+}$*;Tbx5*$^{flox/+}$ mutant embryos (n=4/7)
173 compared to controls (n=0/3), at E14.5 (Supp. Figure 3A-C). This result contrasted with a previous
174 report that did not identify VSDs, albeit using a mixed genetic background [22]. This provided
175 evidence that appropriate *Tbx5* dosage in the IVS was essential for proper ventricular septation.
176
177 <u>Disturbed septal lineage contributions from reduced *Tbx5*.</u> As TBX5 dosage reduction globally or
178 only in the IVS results in VSDs, we reasoned that reducing TBX5 dosage may affect the regulation
179 of the *Tbx5*$^{+}$*/Mef2cAHF*$^{+}$ septal progenitors and their subsequent lineage contributions. We
180 evaluated a reduction of *Tbx5* using a hypomorphic (*Tbx5*^{CreERT2}) allele [18] in combination with a

conditional deletion of *Tbx5* (*Tbx5*^{flox}) [19] at E6.5. This resulted in levels of *Tbx5* that are estimated to be about 25% of wildtype in the *Tbx5*$^{+}$ lineage. In control (*Tbx5*$^{CreERT2/+}$*;Mef2cAHF-DreERT2;Rosa26*$^{Ai66/Ai6}$) embryos, the *Tbx5*$^{+}$*/Mef2cAHF*$^{+}$ septal lineage overlapped at the lineage front of the *Tbx5*$^{+}$ lineage in the IVS, from the base to the apex of the heart at the IV groove, spanning from anterior to posterior of the heart in the IVS (Figure 4A-A", Supp. Figure 4A, B). Among *Tbx5*$^{CreERT2/flox}$ mutant (*Tbx5*$^{CreERT2/flox}$*;Mef2cAHF-DreERT2;Rosa26*$^{Ai66/Ai6}$) embryos, we found that reduced TBX5 dosage at E6.5 caused a spectrum of defects, frequently including VSDs, ASDs and AVC defects at E14.5 (Figure 4B-D'), reminiscent of features of Holt-Oram Syndrome [16,17,23]. The normally organized distribution of the tdTomato^{+} cells was highly irregular in the *Tbx5*$^{CreERT2/flox}$ mutant hearts regardless of VSDs (Supp. Figure 4A-H). Often, tdTomato^{+} cells were less apparent in the posterior IVS (Figure 4A', A", B', B", C', C", D'), and tdTomato^{+} cells were nearly absent in a heart that displayed a severe AVC defect and chamber hypoplasia (Figure 4D, D', Supp Figure 4G, H).

We used quantitative morphometry to assess the position and distribution of the *Tbx5*$^{+}$*/Mef2cAHF*$^{+}$ septal lineage at the IVS. We tested this by quantifying linear profiles of the labeled *Tbx5*$^{+}$*/Mef2cAHF*$^{+}$ septal lineage in the heart. We found that both distribution and position of the *Tbx5*$^{+}$*/Mef2cAHF*$^{+}$ septal lineage was disturbed in *Tbx5*$^{CreERT2/flox}$ mutant (n=3; control, n=4)(Figure 4E-H, Supp. Figure 4I, J), including an increase of tdTomato^{+} cells leftward in the LV, suggesting abnormal lineage position. As well, we observed a broader band of *Tbx5*$^{+}$*/Mef2cAHF*$^{+}$ septal lineage cells, suggesting that proper TBX5 dosage maintains integrity of the compartment boundary marked by the *Tbx5*$^{+}$*/Mef2cAHF*$^{+}$ lineage at the IVS (Figure 4G, H). We also observed a reduction, or sometimes absence, of the labeled septal lineage in AVC cells, as well as remnant atrial septal tissue in *Tbx5*$^{CreERT2/flox}$ mutants (Figure 4D, D').

We further observed that cells of the *Tbx5*$^{+}$*/Mef2cAHF*$^{+}$ lineage in the IVS were arranged like a stack of coins, especially from the apex to the mid-septum (Figure 4A"). We wondered if proper TBX5 dosage might be necessary for maintaining appropriate cell orientation in the IVS.

Therefore, cell alignment was determined and quantified by two metrics, average orientation score or directional coherency. In *Tbx5*$^{CreERT2/flox}$ mutant hearts, *Tbx5*$^{+}$/*Mef2cAHF*$^{+}$ lineage (tdTomato^{+}) and *Tbx5*$^{+}$ lineage (ZsGreen^{+}) cells were reduced in the dominant direction of cell orientation and were more frequently in the orientation orthogonal to the dominant direction (Figure 4S, Supp. Figure 4T). Further, both lineages demonstrated worse directional coherency in *Tbx5*$^{CreERT2/flox}$ mutants (Figure 4T, Supp. Figure 4U), implicating TBX5 in proper cell orientation in the IVS.

<u>*Tbx5*-sensitive genes encode guidance cues</u>. To find downstream effectors of Tbx5 that may mediate the regulation of *Tbx5*$^{+}$/*Mef2cAHF*$^{+}$ lineage cells, we applied single cell RNA sequencing at E13.5, prior to completion of ventricular septation. We micro-dissected the RV, LV and IVS+AVC in controls (*Tbx5*$^{CreERT2/+}$*;Mef2cAHF-DreERT2;Rosa26*$^{Ai66/Ai6}$) (n=4) and *Tbx5* mutants (*Tbx5*$^{CreERT2/flox}$*;Mef2cAHF-DreERT2;Rosa26*$^{Ai66/Ai6}$) (n=2) (Figure 5A). These samples were labeled at E6.5 for progenitors of the *Tbx5*$^{+}$/*Mef2cAHF*$^{+}$ lineage (*tdTomato*$^{+}$) and *Tbx5*$^{+}$ lineage (*ZsGreen*$^{+}$). In samples from each cardiac tissue region, we detected clusters enriched for *Tnnt2*$^{+}$ cardiomyocytes (CMs), *Postn*$^{+}$ fibroblasts, *Plvap*$^{+}$ endothelial cells, *Tbx18*$^{+}$/*Wt1*$^{+}$ epicardial cells, *Hbb-b2*$^{+}$ red blood cells, and *C1qb*$^{+}$ white blood cells (Figure 5B, Supp. Figure 5A-F).

In particular, *tdTomato*$^{+}$ cells were most abundant among clusters of *Tnnt2*$^{+}$ cardiomyocytes (CMs) of the IVS+AVC region (Figure 5C). However, we were unable to identify a gene expression signature that was unique to the *Tbx5*$^{+}$/*Mef2cAHF*$^{+}$ lineage, beyond the lineage marker itself, at this stage. Likewise, *ZsGreen*$^{+}$ cells were also enriched among clusters of *Tnnt2*$^{+}$ CMs in this region (Figure 5D), indicative of the *Tbx5*$^{+}$ lineage contribution to CMs in the region, as well as a site of conditional reduction of *Tbx5* among *Tbx5* mutants.

We then focused our analysis on a subset of *Tnnt2*$^{+}$ enriched clusters from IVS+AV canal regions. We identified genotype-enriched clusters that were abundant with cells from controls (Cluster 5) or *Tbx5* mutants (Cluster 10) (Figure 5E, F). Control-enriched cluster 5 included genes

expressed in the AV canal region, encoding the Wnt co-receptor *Rspo3*, morphogen *Bmp2*, and transcription factors *Tbx2* and *Tbx3*, suggesting that these genes are reduced in *Tbx5* mutants (Figure 5G, H). As well, the SLIT-receptor *Robo1,* which is implicated in mouse and human VSDs [24–26], and Netrin-receptor *Unc5b,* were also downregulated in *Tbx5* mutant cells (Figure 5G, H).

In the mutant-enriched cluster 10, genes typically expressed in ventricular trabeculae were enriched (Figure 5G, H). These included natriuretic peptide *Nppa*, transcription factor *Cited1,* and bone morphogenetic protein *Bmp10*, suggesting ectopic expression of these trabecular genes in the IVS of *Tbx5* mutants. Intriguingly, guidance cues *Netrin1* (*Ntn1)* and *Slit2,* which are best known for axonal development or vasculogenesis [27], were also dysregulated (Figure 5G, H).

We examined differential gene expression between controls or *Tbx5* mutants in *tdTomato*$^+$ (Tbx5$^+$/Mef2cAHF$^+$ septal lineage) or *ZsGreen*$^+$ (Tbx5$^+$ lineage) CMs. We found many differentially expressed genes that overlapped among comparisons of *tdTomato*$^+$ or *ZsGreen*$^+$ clusters, including *Nppa*, *Cited1,* and *Slit2*, consistent with findings from cluster-to-cluster comparisons (Supp. Figure 5G, H).

We used orthogonal assays to validate candidate TBX5-sensitive genes. By fluorescence *in situ* hybridization in formalin fixed paraffin embedded (FFPE) sections, we observed a reduction of gene expression of *Bmp2, Robo1 and Unc5b* in the AV canal region of mutant hearts when compared to controls. (Supp. Figure S6M-X'). As well, we detected expansion of gene expression of *Nppa* and *Slit2* in the IVS and compact layer of mutant hearts, both of which are normally expressed only in the trabecular regions of both ventricles of control hearts (Figure 5I-L'). Moreover, we discovered *Ntn1* expression enriched in LV trabeculae and in a gradient across the control IVS (Figure 5M, M'), consistent with immunostaining of NTN1 in the heart at E14.5 (Supp. Figure 6Y). Notably, *Ntn1* was enriched in the LV earlier at E11.5 during ventricular septation (Supp. Figure 6Z). However, in *Tbx5* mutants, the *Ntn1* gradient was flattened and expanded in the IVS by reduced Tbx5 dosage (Figure 5N, N'). Interestingly, we observed changes of *Nppa*, *Slit2* and *Ntn1* in *Tbx5* mutants with or without VSDs, suggesting that this dysregulated gene

expression was not secondary to VSDs (Supp Figure 6A-L'). In addition, analysis of ChIP-seq of TBX5 from embryonic mouse hearts [28] showed TBX5 occupancy at promoters of *Nppa, Slit2*, and *Ntn1* (Supp Figure 7A-C), suggesting these guidance genes are likely to be direct targets of TBX5 in the heart.

<u>*Tbx5-Slit2* and *Tbx5-Ntn1* genetic interactions.</u> We evaluated if genetic interactions existed between *Tbx5* and *Slit2* or *Ntn1*. As *Tbx5* heterozygous mutant (*Tbx5*$^{del/+}$)[19] mouse embryos display muscular or membranous VSDs, we wondered if heterozygous *Slit2* or *Ntn1* loss of function (LOF) mutant embryos might alter *Tbx5*-dependent phenotypes. We mated *Tbx5*$^{del/+}$ mice with either *Slit2* (*Slit2*$^{+/-}$) or *Ntn1* (*Ntn1*$^{beta\text{-}actin\text{-}Cre/+}$ referred here subsequently as *Ntn1*$^{+/-}$[29,30]) heterozygous LOF mice. In *Tbx5*$^{del/+}$ embryos at E14.5, we observed membranous (n=5/8) or muscular (n=3/8) VSDs by histology (Supp. Figure 8B, E), consistent with previous reports [19]. Among *Slit2*$^{+/-}$ embryos at E14.5, we observed a membranous VSD (n=1/8) (Supp. Figure 8C, E). This contrasted with a previous report that did not detect any VSDs in *Slit2*$^{+/-}$ albeit using a different mutant *Slit2* allele [24]. In *Tbx5*$^{del/+}$;*Slit2*$^{+/-}$ compound heterozygous embryos, we observed an estimated decrease in the incidence of membranous VSDs (n=5/8) (Supp. Figure 8D, E), which approached significance (log OR -2.5; $p<0.09$ in a Generalized Linear Model).

We next tested if there was a genetic interaction between *Tbx5* and *Ntn1* (Supp. Figure 8F-J). In *Ntn1*$^{+/-}$embryos, we observed a membranous (n=1/9) or a muscular (n=1/9) VSD. In *Tbx5*$^{del/+}$;*Ntn1*$^{+/-}$ compound heterozygous embryos, we observed a significant decrease of membranous VSDs (n=1/8; log OR -5.3; $p<1x10^{-3}$ by a Generalized Linear Model), but not significant changes to prevalence of muscular VSDs (n=4/8; log OR 0.12; $p<0.93$), consistent with a genetic interaction between *Tbx5* and *Ntn1* for ventricular septation.

We wondered if there were other quantitative histologic differences, in addition to the changes in incidence of VSD types. To quantify morphometry from histology, we leveraged a deep learning algorithm, known a CODA [31], to detect embryonic mouse heart components from

hematoxylin and eosin (H&E) sections. We generated three-dimensional (3-D) tissue reconstructions, to visualize and quantify anatomic structures and CHDs, including membranous and muscular VSDs, at cellular resolution (Figure 6I-K). Using this machine learning method, we discovered that the cell density of the IVS, which we termed IVS fill, was increased in *Tbx5*$^{del/+}$; *Ntn1*$^{+/-}$ embryos compared to wildtype ($p<0.05$ by Fisher's exact test), while classification of the IVS as trabecular was significantly reduced in *Tbx5*$^{del/+}$;*Ntn1*$^{+/-}$ embryos ($p<0.05$ by Fisher's exact test) (Supp. Figure 8M). In addition, we estimated the minimal area for each membranous or muscular VSD, when present (Supp. Figure 8O, P). In *Tbx5*$^{del/+}$;*Slit2*$^{+/-}$ compound mutants, we detected statistically significant levocardia ($p<0.001$ by Fisher's exact test), as determined by the axis of the heart compared to the spine and sternum (Supp. Figure 8Q). This uncovered a genetic interaction between *Tbx5* and *Slit2* related to heart position, demonstrating that machine learning-based morphometry can quantify unexpected anatomic findings.

<u>*Slit2* and *Ntn1* for ventricular septation.</u> To determine if *Slit2* or *Ntn1* are essential for ventricular septation, we evaluated homozygous LOF mouse mutants for *Slit2* or *Ntn1* for VSDs. In *Slit2*$^{-/-}$ embryos at E14.5, we observed that homozygous loss of *Slit2* displayed complete penetrance for VSDs, including membranous (n=4/4; log OR 5.0, $p<0.00$) or muscular VSD (n=1/4) (Figure 6A-D), demonstrating a far higher incidence than a previous report using an alternative *Slit2* LOF allele [24]. Further, we detected statistically significant a non-compacted IVS as determined by reduced IVS fill and thinning of the right ventricular compact layer (Supp. Figure 9E, H). Likewise, *Ntn1*$^{-/-}$ embryos displayed membranous VSDs (n=6/7), an apparent thinning of the ventricular compact layer and a non-compacted IVS, although these observations were not statistically significant (Supp. Figure 9). Collectively, this morphologic evidence implicates *Slit2* and *Ntn1* in proper ventricular septation during heart development.

As *Slit2* and *Ntn1* were necessary for ventricular septation, we asked if loss of *Slit2* or *Ntn1* might disturb distribution of the Tbx5^{+}/Mef2cAHF^{+} lineage in the IVS. In homozygous *Slit2* LOF mutants with the lineage reporter (*Tbx5*$^{CreERT2/+}$;*Mef2cAHF-DreERT2*;*ROSA26*$^{Ai66/+}$;*Slit2*$^{-/-}$) (n=4), we observed a statistically-significant broadened distribution of the Tbx5^{+}/Mef2cAHF^{+} lineage compared to controls (n=2) (Figure 6N-Q), consistent with lineage mixing from boundary disruption and implicating a role for SLIT2 in maintaining boundary integrity. Conversely, homozygous *Ntn1* LOF mutants with the lineage reporter (*Tbx5*$^{CreERT2/+}$;*Mef2cAHF-DreERT2*; *ROSA26*$^{Ai66/+}$;*Ntn1*$^{-/-}$) (n=6) demonstrated leftward displacement of the Tbx5^{+}/Mef2cAHF^{+} lineage compared to controls (n=4) (Figure 6R-U), implying that NTN1 signaling precisely positions the compartment boundary at the IVS. Taken together, this evidence suggested that SLIT2- and NTN1-signaling, as part of a Tbx5-dependent pathway, regulates the position and integrity of the compartment boundary labeled by the Tbx5^{+}/Mef2cAHF^{+} lineage.

Discussion.

We show that *Tbx5*$^{+}$/*Mef2cAHF*$^{+}$ progenitors prefigure a compartment boundary that becomes located at the junction between the left and right sides of the IVS, providing a cellular framework during development for heart patterning. Our study underscores a fundamental principle that early developmental events preconfigure structure and function of the heart and are susceptible to genetic risks that cause CHDs.

Compartment boundaries have been defined by several criteria. First, a compartment boundary segregates juxtaposed cell populations such as distinct cell lineages to restrict cell intermingling, and ablation of the boundary leads to cell mixing. Second, the expression domain of a selector gene corresponds with a compartment domain, loss of the selector gene eliminates the identity in this territory, and ectopic expression of the selector induces this identity. Third, a selector gene establishes a signaling center to maintain the compartments and boundary. Our results satisfy all of these criteria: Ablation of the *Tbx5*$^{+}$/*Mef2cAHF*$^{+}$ lineage disrupts segregation

of *Tbx5*$^{+}$ lineage cells in the LV from the *Tbx5*$^{-}$ lineage in the RV of the developing heart. Reduced *Tbx5* expression impairs the integrity of the boundary and its patterning, and in previous work misexpression of TBX5 eliminates IVS formation [21]. Third, TBX5 patterns signaling molecules that are important for morphologies that impact the boundary. In this context, we postulate that *Tbx5* may function as a candidate selector gene. Further experiments will be needed to formally ascertain this.

In this context, we identify a *Tbx5*-dependent pathway that regulates *Slit2* and *Ntn1*. Normally, TBX5 represses their ectopic expression in the IVS and compact layer. Both SLIT2 and NTN1 are guidance or adhesive cues in several developmental contexts. Here, we provide evidence that *Slit2* and *Ntn1* are direct targets of TBX5, and that *Tbx5* and *Slit2* or *Ntn1* genetically interact. Further, we found that *Slit2* and *Ntn1* are essential for proper ventricular septation, as well as compartment boundary integrity and positioning, respectively. Like TBX5, proper ventricular septation may be sensitive to imbalanced dosage of SLIT2 or NTN1. As *Ntn1* expression is enriched in the LV and left-side of the IVS in the *Tbx5*$^{+}$ compartment, we propose a working hypothesis that NTN1 functions as a TBX5-dependent signaling center for compartment boundary regulation.

The spatiotemporal position of the boundary is at the crux of cardiac septation and, when disrupted, spans sites for congenital cardiac anomalies. The sensitivity of the *Tbx5*$^{+}$/*Mef2cAHF*$^{+}$ lineage-labeled boundary to genetic perturbations, specifically *Tbx5* deficiency, is of significance in the context of congenital heart disease. Such deficiency selectively compromises the boundary's integrity and position, along with disturbances to cell orientation, leading to VSDs or AVSDs. This observation suggests that genetic pathways for patterning, like the *Tbx5*$^{+}$/*Mef2cAHF*$^{+}$ lineage-labeled boundary, can be exceptionally susceptible to genetic disruptions. Whether additional genetic perturbations that cause VSDs or AVSDs disrupt the compartment boundary remains to be determined. Likewise, it will be interesting to evaluate if the *Tbx5*$^{+}$/*Mef2cAHF*$^{+}$ lineage-labeled boundary corresponds with abnormal shifts in IVS position, like

those observed in the endothelial loss of *Hand2*, which displays rightward shifted IVS and double inlet left ventricle (DILV) or two IVS primordia [32,33].

In conclusion, our research demonstrates the delicate interplay of progenitor cell behavior, gene expression and boundary formation that determines heart development and genetic susceptibility that increases the risk of CHDs. This evidence further underscores the significance of early developmental stages for the ontogeny of some CHDs. The implications of these discoveries likely extend beyond cardiac morphogenesis, as these findings offer insights for the roles of compartment boundaries during mammalian development and uncover a vulnerability for organ patterning from genetic disturbances.

METHODS.

Mouse lines. All mouse protocols were approved by the Institutional Animal Care and Use Committee at UCSF. Mice were housed in a barrier animal facility with standard husbandry conditions at the Gladstone Institutes. Mice of *Tbx5*^{CreERT2IRES2xFLAG} (abbreviated here as *Tbx5*^{CreERT2}) and *Mef2cAHF-DreERT2* [6], *Tbx5*$^{del/+}$ and *Tbx5*$^{flox/+}$ [19], *ROSA26*^{Ai66} and *ROSA26*^{Ai6} [14] were described previously. *Mef2cAHF-Cre*$^{/+}$ mice [20] were obtained from Brian Black. *Slit2*$^{+/-}$ mice (MMRC, Strain 065588-UCD, donated by Kent Lloyd) were generated by CRISPR/Cas9-targeted constitutive deletion of exon 8 and flanking splicing regions of *Slit2*. *Ntn1*$^{+/-}$ mice were derived from matings of *Ntn1* floxed mice (*Ntn1*$^{flox/+}$; Jackson Laboratory #028038) [34] to beta-actin-Cre [30], which were obtained from Gail Martin. All mouse strains were maintained in the C57BL6/J background (Jackson Laboratory #664), except for *Tbx5*$^{del/+}$, which was maintained in Black Swiss (Charles River, Strain Code 492), and *Slit2*$^{+/-}$ which was maintained in C57BL6/N (Jackson Laboratory, #005304). Both male and female embryos were collected from timed matings and used at random for experiments.

Cloning and generation of mouse lines.

We generated an attenuated diptheria toxin (DTA176) transgenic knock-in mouse under the control of the dual-recombinase intersectional cassette. DTA176 encodes an attenuated form of toxic fragment A from diptheria toxin [15], which requires ~100-200 molecules for cell killing. This strategy was an effort to reduce potential problems of leaky DTA expression prior to recombinase-mediated activation. Briefly, DTA176 [15] was cloned downstream of ROX-STOP-ROX and LOX-STOP-LOX sites to create a Dre- and Cre-dependent expression construct, which was derived from the Dre- and Cre-dependent tdTomato expression cassette of the Ai66 (RCRL-tdT) targeting vector [14]. After the tdTomato cassette was removed using MluI sites and replaced by DTA176, the construct was cloned into the TARGATT targeting construct pBT346.3 (Applied Stem Cells) to target the transcriptionally inactive *Hip11* locus [35] using PacI and SmaI restriction enzyme sites. The final construct was verified using restriction digestion and Sanger sequencing. DNA was purified and injected along with mRNA for the Phi31o transposase according to manufacturer's protocol to generate intersectional-DTA mutant (*Hip11*$^{Rox\text{-}STOP\text{-}Rox\text{-}Lox\text{-}STOP\text{-}Lox\text{-}DTA176}$) mice. To generate Ai66b mice (*ROSA26*^{Ai66b}), which is a Dre-dependent tdTomato reporter, the LOX-STOP-LOX sites were removed from the Ai66 (RCRL-tdT) targeting vector [14], and then the transgene cassette was inserted into endogenous genomic loci via homologous recombination, as previously described [36].

<u>Whole mount embryo and heart immunofluoresence labeling</u>

Embryos were dissected from timed pregnant dams, including removal of yolk sac with genotyping, as previously described [6]. Embryos up to E10.5 were fixed for 4 hours with 4% PFA at room temperature, then incubated with gentle rocking in clearing solution (8% SDS in 0.2M borate buffer) at 37°C for 1-3 hours until clear. E13.5 or E14.5 hearts were micro-dissected from freshly harvested embryos in PBS with heparin (10 Units/mL) (Sigma #H3393) or incubated in 1X RBC lysis solution (Roche #11814389001) for 10 minutes at room temperature, fixed at room temperature in 4% PFA for one hour, and incubated with gentle rocking in clearing solution at

37°C for 2-4 days until clear. Specimens were permeabilized and blocked for two hours to overnight with gentle rocking at 37°C in blocking buffer (PBS containing 5% normal donkey serum and 0.8% to 1.5% Triton X-100, dependent on embryo/heart stage). Specimens were labeled with primary antibody (list below) in blocking buffer with gentle rocking at 37°C, overnight for embryos up to E10.5, or 5 days for E13.5 or E14.5 hearts with fresh antibody replaced mid-way. Following three washes in blocking buffer, each 45 minutes except the third overnight for E13.5 and E14.5 hearts, specimens were labeled with secondary antibody (raised in donkey; AF488-, Dy405-, Cy3, or AF647-conjugated; used at 1:750; Jackson ImmunoResearch) and DAPI in blocking buffer with gentle rocking at 37°C, 2-3 hours for embryos up to E10.5, or 5 days for E13.5 or E14.5 hearts. Following three washes in PBS with gentle rocking at 37°C, samples were stored (up to overnight) in PBS with 0.2% sodium azide. Primary antibodies used were: tdTomato (rabbit, Rockland 600-401-379, 1:1000), MEF2c (R&D AF6786, sheep, 1:250), TNNT2 (mouse, Thermo MS-295-P, 1:500). Strong ZsGreen fluorescence persisted after clearing and did not require immunolabeling.

Lightsheet Image Acquisition

Images were acquired by lightsheet microscopy, as described previously [37]. Brielfy, specimens were warmed and transferred to 2% low melting point agarose (Fisher BP165-25) in PBS at 37°C, then embedded in glass capillary tubes with paired pistons (Sigma Z328510 paired with BR701938, or Sigma Z328502 paired with BR701934) for embryos, or tip-truncated 1mL syringes (Becton Dickinson) for hearts. After the gel solidified, the capillaries or syringes were suspended specimen-down from 14mL polystyrene tubes sealed with Parafilm. Columns containing the specimen were partially extended into an ample volume optical clearing solution (OCS, EasyIndex EI-Z1001, LifeCanvas). Following overnight incubation in OCS, specimen capillaries were retracted and were brought to a Light Sheet Z.1 microscope coupled with ZEN software (Carl Zeiss Imaging). With immersion in OCS, specimens were rotated and imaged from multi-view whole-volume approach, to improve fluorescence signal intensity and resolution captured

throughout the entire heart volume. One of two objective setups was used: EC Plan Neofluar 5X/0.16 with 5X/0.1 pair (hearts), or Clr Plan Neofluar 20X/1.0 paired with 10X/0.2 clearing pair (embryos). Z-stacks were collected at each view angle at the optimal slice thickness determined by Zeiss' Zen software, ranging from 1.42 to 4.95 µm.

Image Dataset Preprocessing

Imaging data was processed, as previously described [37]. All data processing was performed on an 8-core x86-64 desktop PC with 64GB RAM, running Kubuntu 20.04 LTS, principally using Fiji software [38]. Acquired light sheet image stacks were subjected to single-view deconvolution using regularized generalized Tikhonov filtering (Parallel Spectral Deconvolution, https://imagej.net/plugins/parallel-spectral-deconvolution) following theoretical PSF calculation using the intersection of Gaussian z-plane illumination with Gibson-Lanni widefield epifluorescence detection patterns [39]. Deconvolved stacks were co-registered, and image volumes were generated for each desired orientation, for each specimen, using Content Based Fusion in BigStitcher [40]. TrackMate [41] and ImageJ 3-D viewer were leveraged for segmentation and visualization of fused volumes. Macros for the batch automation of these steps are available upon request.

Image Volume Quantification

Extensive whole-volume quantifications of imaged E14.5 hearts were performed using Fiji and associated plugins, with analysis conducted with R statistics. For assessing the location of fluorescence signal, volumes were downsampled, and 2-dimensional regions of interest (ROIs) corresponding to anatomic structures were manually drawn on each Z-slice, using the DAPI channel. Integrated intensity for each fluorescence channel was programatically measured for each ROI, and counts were normalized to DAPI signal and pooled by anatomic region. For whole-

heart quantifications, counts were further normalized to combined Ai6 plus Ai66 signal, then and averaged across each anatomic region. For orientation assessments, a multi-channel panel of 174 full resolution four-chamber image excerpts were blinded, selected and evenly distributed between apical posterior, apical anterior, posterior basal, and posterior apical IVS, split by channel (tdTomato or ZsGreen) and sampled. Using automated batch processing, samples were subjected to background filtering, contrast enhancement, and measurements of orientation distribution and dominant direction (OrientationJ plugin, https://github.com/Biomedical-Imaging-Group/OrientationJ), and of directionality (Directionality plugin, https://github.com/fiji/Directionality). Orientation score distributions were rotated so that dominant direction was at 0°, and average score (across the panel of images) was plotted as a function of direction and examined by Watson's two-sample test. Individual scores surrounding 0° and 90° were pooled and compared with the Wilcoxon signed-rank test. Directionality coherence scores (across the panel of images) were plotted by genotype and compared with the Wilcoxon signed-rank test. Macros for the batch automation of these steps are available upon request.

Quantification of right-left position of lineages.

For each E10.5 heart analyzed, five representative coronal optical sections were selected, approximately 20-35 μm apart. For each optical section, the DAPI channel was used to draw five linear profiles spanning the ventricular chambers from right to left. Linear profiles were drawn such that the "0" position corresponded to the midline, identified by the interventricular groove. Fluorescence intensity of each channel (green=*Tbx5*$^{+}$ lineage, magenta=*Mef2cAHF*+ lineage) was measured along each linear profile, and intensity values were normalized to the maximum value along each profile. Profiles for each channel were grouped by experimental condition (WT or DTA), and then the average ± SEM normalized fluorescence intensity profiles were calculated and plotted. Welch's two-sample t-test was used at each position along the right-left axis to

determine regions of significant difference in fluorescence intensity of each channel between experimental groups, indicating a change in the distribution of cells of that lineage.

For each E13.5-E14.0 heart analyzed, maximum z-projections were generated from optical sections spanning every 50 µm from the anterior to posterior of the heart. For each maximum z-projection, the DAPI and red or magenta (*Tbx5*$^{+}$/*Mef2cAHF*$^{+}$ intersectional lineage) channels were split and background subtraction was performed on the red or magenta channel using a 50-pixel rolling ball radius. The DAPI channel was used to draw three linear profiles (basal, middle, apical) spanning the ventricular chambers from right to left. Linear profiles were drawn such that the "0" position corresponded to the middle of the IVS. Fluorescence intensity of the red or magenta channel was measured along each linear profile, and intensity values were normalized to the maximum value along each profile. Profiles were grouped by experimental condition (*Tbx5*$^{CreERT2/+}$ or *Tbx5*$^{CreERT2/flox}$) or (e.g. WT, *Ntn1*$^{+/-}$, *Ntn1*$^{-/-}$) and then the average ± SEM normalized fluorescence intensity profiles were calculated and plotted. Welch's two-sample t-test was used at each position along the right-left axis to determine regions of significant difference in fluorescence intensity between experimental groups, indicating a change in the distribution of *Tbx5*$^{+}$/*Mef2cAHF*$^{+}$ intersectional lineage cells.

Cell Harvesting for Single Cell RNA Sequencing

Samples for single cell RNA sequencing were collected from three independent litters at E13.5. The heart was microdissected to obtain the interventricular septum (IVS), left ventricular (LV) and right ventricular (RV) regions. Each microdissected tissue was singularized with TrypLE Express (Life Technologies, Cat# 12604-013) at 37C and quenched with 1% FBS in PBS. The single cell suspension was then filtered through a cell strainer cap (Corning, Cat# 352235) and centrifuged at 300g for 5 minutes. The pellet was resuspended in 1% FBS in PBS and counted using an automated cell counter. A 30µL aliquot of the cell suspension was used to generate single cell droplet libraries with the Chromium Next GEM Single Cell 5' Library & Gel Bead Kit v1.1,

according to manufacturer's instructions (10X Genomics). After KAPA qPCR quantification, a shallow sequencing run was performed on a NextSeq 500 (Illumina) prior to deep sequencing on a NovaSeq S4 (Illumina).

Data Processing Using Cellranger

All datasets were processed using Cellranger 2.0.2. FASTQ files were generated using the mkfastq function. Reads were aligned to a custom mm9 reference (version 1.2.0) containing tdTomato and ZsGreen reporter genes. Cellranger aggr was used to aggregate individual libraries after read depth normalization.

Seurat Analysis

Outputs from the Cellranger pipeline were analyzed using the Seurat v3 [42–44]. Datasets from the IVS, LV and RV were analyzed separately. Cells with 10,000-50,000 UMIs and 1500-7250 genes were retained. Data was normalized using the NormalizeData function and scaled using ScaleData, while also regressing unwanted sources of variation, such as differences in the number of UMIs, number of genes, percentage of mitochondrial reads and differences between G2M and S phase scores. Principal component analysis (PCA) was performed using the most highly variable genes. Cells were then clustered based on the top 30 principal components and visualized on a Uniform Manifold Approximation and Projection (UMAP) [45]. A clustering resolution that separated cells by major cell types was chosen. Next, *Tnnt2*$^{+}$ clusters from the IVS dataset were extracted and re-clustered, similar to the parent dataset above. A clustering resolution was chosen based on separation of genotypes. Differential gene expression tests between clusters or between *ZsGreen*$^{+}$ and *ZsGreen*$^{-}$ or *tdTomato*$^{+}$ and *tdTomato*$^{-}$ cells were performed using the FindMarkers function with default parameters. Selected differentially expressed genes with an adjusted p-value less than 0.05 from the Wilcoxon rank sum test were displayed using the Dotplot or FeaturePlot functions.

Fluorescent *In Situ* Hybridization

E11.5 or E14.5 hearts were fixed with 4% paraformaldehyde or 10% formalin overnight at 4C, embedded in paraffin and then sectioned for a transverse or four-chambered view on slides. *In situ* hybridization was performed on sections using the RNAscope Multiplex Fluorescent v2 Assay kit (Advanced Cell Diagnostics, Cat# 323100). Briefly, sections were deparaffinized in xylene and 100% ethanol, treated with hydrogen peroxide for 10 minutes and boiled in target retrieval buffer for 10 minutes. A hydrophobic barrier was drawn around each section using an Immedge pen (Vector Laboratories, Cat# H-4000), and slides were allowed to dry overnight. The following day, sections were treated with Protease Plus for 30 minutes, followed by hybridization with probes for 2 hours at 40C. Probes used were *Mm-Tnnt2-C4* (Cat# 418681-C4), *Mm-Ntn1* (Cat# 407621), *Mm-Slit2* (Cat# 449691), *Mm-Nppa-C3* (Cat# 418691-C3), *Mm-Bmp2-C2* (Cat# 406661-C2), *Mm-Robo1* (Cat# 475951) and *Mm-Unc5b* (Cat# 482481). Amplification steps were carried out according to manufacturer's instructions. Opal dyes 520, 570, 620 and 690 (Akoya Biosciences, Cat# FP1487001KT, FP1487001KT, FP1487001KT and FP1487001KT) were used at 1:750 dilution. After staining with DAPI, 1-2 drops of ProLong Gold Antifade Mountant (ThermoFisher Scientific, Cat# P36930) were placed on the slides and mounted with a coverslip. Slides were stored overnight at 4C and were imaged at 10X magnification on the Olympus FV3000RS. Multi-Area Time Lapse (MATL) images were captured and then stitched together using the Olympus FV3000RS software. Stitched images were analyzed using ImageJ OlympusViewer plugin.

Immunohistochemistry

Cryopreserved slides were thawed from -80C at RT and washed in 0.1% Triton X-100 in PBS (PBST) for 3 x 5 min. Antigen-retrieval was performed by boiling slides in 10mM sodium citrate buffer (pH 6.0) for 10 minutes and then washed in H2O for 3 x 5 min. Blocking was performed using 5% donkey serum in 0.1% PBST at RT for 1-2hr. Anti-Netrin-1 antibody 1:500 (R&D

Systems AF1109) in 1% BSA + 0.1% PBST was incubated at 4C overnight. After washing 3 x 5 min in 0.1% PBST, slides incubated in Alexa Fluor 594 (1:300) in 1% BSA + 0.1% PBST at RT for 1 hr. Slides were then washed 3 x 5 min in 0.1% PBST and incubated in 1:1000 DAPI in 0.1% PBST at RT for 5-10 minutes. Finally, slides washed 3 x 5 min in 0.1% PBST, glass coverslips were mounted using Prolong Gold antifade mounting medium and stored at 4C.

Machine learning-based 3-D reconstruction from histology and quantitative micrometry

Tissues were formalin-fixed, paraffin embedded (FFPE) and serially sectioned at a standard thickness of 5 μm to exhaustively collect the heart tissue of each fetal mouse. Serial sections were stained with hematoxylin and eosin (H&E) and digitized at 20x magnification. CODA, a technique to 3-D reconstruct serial tissue images, was used to map the microanatomy of the hearts [31,46]. The various steps of CODA can be broken down into image registration, nuclear detection, and tissue labelling. Nonlinear image registration was used to align the serial images. Cellular coordinates were generated through color deconvolution and detection of two-dimensional intensity peaks in the hematoxylin channel of the images. A deep learning semantic segmentation algorithm was trained to label the anatomical structures of the mice at 1 μm resolution. To train the model, manual annotations of six structures were generated in 55 histological images corresponding to the different large structures present in the tissue: bones, spinal cord, lung, liver, stroma, heart, and non-tissue pixels in the images. A second deep learning model was trained to subclassify the regions of interest within the heart: compact myocardium, trabeculae, IVS, AV canal and atria. Fifty images from the manual annotation datasets were used for model training, with five images held out for independent testing of model accuracy. The models were deemed acceptable when they reached a minimum per-class precision and recall of >85%. Using the trained model, independent images were segmented and aligned to generate digital 3-D datasets.

The reconstructed volumes enabled microanatomical quantification of anatomical properties. IVS fill, or the solidity of the muscle layer in the IVS, was calculated by dividing the number of dark (<200 in RBG color space) pixels within the IVS, normalized by all pixels (including empty space) within the IVS. Percent trabeculation within the IVS was calculated by first isolating the tissue classified as trabeculae that was spatially attached to the IVS, then normalizing this number by the combined volume of trabeculae attached to IVS and the volume of the IVS itself. The compact myocardium thickness was calculated by measuring the thickness of the compact layer at the bottom 20% of the ventricles. To measure the thickness on the left and right ventricles, the two sides of the heart were manually segmented in 3-D space. VSDs were identified by calculating regions where the empty space of the left ventricle contacted the empty space of the right ventricle. These defects were evaluated and manually sorted into membranous or muscular sub-types. The areas of each defect were then manually calculated through annotation on serial histological images representing the shortest path to close the defect. These lines were summed across all images containing the defect multiplied by the thickness of the histological slides to determine the area of the hole.

Quantification and Statistical Analysis

For statistical analysis of genetic interactions, the number of animals with a given defect (muscular VSD or membranous VSD) was modeled in a Generalized Linear Model assuming a binomial probability distribution for the observed counts. This model included main effects (in terms of log odds ratios) capturing the number of mutant alleles for *Tbx5* (0 or 1, representing the WT or the Het genotype, respectively) and the number of mutant alleles for *Slit2* or *Ntn1* (0,1 or 2: representing the WT, Het or Hom genotype, respectively) and an interaction between these effects. Given the relatively small number of animals in this experiment, bias-reduced estimates were made using the brglm2 package {Kosmidis.2020} in R <https://www.R-project.org/>.

References

1. Cruz, M.V.D.L., Sánchez-Gómez, C., and Palomino, M.A. (1989). The primitive cardiac regions in the straight tube heart (Stage 9) and their anatomical expression in the mature heart: An experimental study in the chick embryo. J Anat *165*, 121–131.

2. Cruz, M.V. de la, Castillo, M.M., G., L.V., Valencia, A., and Moreno-Rodriguez, R.A. (1997). Primitive interventricular septum, its primordium, and its contribution in the definitive interventricular septum: In vivo labelling study in the chick embryo heart. Anatomical Rec *247*, 512–520. 10.1002/(sici)1097-0185(199704)247:4<512::aid-ar10>3.0.co;2-s.

3. Wessels, A., Vermeulen, J.L.M., Virágh, S.Z., Kálmán, F., Morris, G.E., Man, N.T., Lamers, W.H., and Moorman, A.F.M. (1990). Spatial distribution of “tissue-specific” antigens in the developing human heart and skeletal muscle. I. An immunohistochemical analysis of creatine kinase isoenzyme expression patterns. Anatomical Rec *228*, 163–176. 10.1002/ar.1092280208.

4. Wessels, A., Markman, M.W.M., Vermeulen, J.L.M., Anderson, R.H., Moorman, A.F.M., and Lamers, W.H. (1996). The Development of the Atrioventricular Junction in the Human Heart. Circ Res *78*, 110–117. 10.1161/01.res.78.1.110.

5. Lamers, W.H., Wessels, A., Verbeek, F.J., Moorman, A.F., Virágh, S., Wenink, A.C., Groot, A.C.G., and Anderson, R.H. (2018). New findings concerning ventricular septation in the human heart. Implications for maldevelopment. Circulation *86*, 1194–1205. 10.1161/01.cir.86.4.1194.

6. Devine, W.P., Wythe, J.D., George, M., Koshiba-Takeuchi, K., and Bruneau, B.G. (2014). Early patterning and specification of cardiac progenitors in gastrulating mesoderm. eLife *3*, 508. 10.7554/elife.03848.

7. Später, D., Abramczuk, M.K., Buac, K., Zangi, L., Stachel, M.W., Clarke, J., Sahara, M., Ludwig, A., and Chien, K.R. (2013). A HCN4+ cardiomyogenic progenitor derived from the first heart field and human pluripotent stem cells. Nat Cell Biol *15*, 1–10. 10.1038/ncb2824.

8. Lescroart, F., Chabab, S., Lin, X., Rulands, S., Paulissen, C., Rodolosse, A., Auer, H., Achouri, Y., Dubois, C., Bondue, A., et al. (2014). Early lineage restriction in temporally distinct populations of Mesp1 progenitors during mammalian heart development. Nat Cell Biol *16*, 829–840. 10.1038/ncb3024.

9. Meilhac, S.M., Esner, M., Kelly, R.G., Nicolas, J.-F., and Buckingham, M.E. (2004). The clonal origin of myocardial cells in different regions of the embryonic mouse heart. Dev Cell *6*, 685–698.

10. Franco, D., Meilhac, S.M., Christoffels, V.M., Kispert, A., Buckingham, M., and Kelly, R.G. (2006). Left and right ventricular contributions to the formation of the interventricular septum in the mouse heart. Dev Biol *294*, 366–375. 10.1016/j.ydbio.2006.02.045.

11. Dahmann, C., Basler, K., Dahmann, C., and Basler, K. (1999). Compartment boundaries: at the edge of development. Trends Genet *15*, 320–326. 10.1016/s0168-9525(99)01774-6.

12. Kiecker, C., and Lumsden, A. (2005). Compartments and their boundaries in vertebrate brain development. Nat Rev Neurosci *6*, 553–564. 10.1038/nrn1702.

13. Wang, J., and Dahmann, C. (2020). Establishing compartment boundaries in Drosophila wing imaginal discs: An interplay between selector genes, signaling pathways and cell mechanics. Semin Cell Dev Biol *107*, 161–169. 10.1016/j.semcdb.2020.07.008.

14. Madisen, L., Garner, A.R., Shimaoka, D., Chuong, A.S., Klapoetke, N.C., Li, L., van der Bourg, A., Niino, Y., Egolf, L., Monetti, C., et al. (2015). Transgenic Mice for Intersectional Targeting of Neural Sensors and Effectors with High Specificity and Performance. Neuron *85*, 942–958. 10.1016/j.neuron.2015.02.022.

15. Wu, S., Wu, Y., and Capecchi, M.R. (2006). Motoneurons and oligodendrocytes are sequentially generated from neural stem cells but do not appear to share common lineage-restricted progenitors in vivo. Development *133*, 581–590. 10.1242/dev.02236.

16. Basson, C.T., Bachinsky, D.R., Lin, R.C., Levi, T., Elkins, J.A., Soults, J., Grayzel, D., Kroumpouzou, E., Traill, T.A., Leblanc-Straceski, J., et al. (1997). Mutations in human TBX5 [corrected] cause limb and cardiac malformation in Holt-Oram syndrome. Nat Genet *15*, 30–35. 10.1038/ng0197-30.

17. Li, Q.Y., Newbury-Ecob, R.A., Terrett, J.A., Wilson, D.I., Curtis, A.R., Yi, C.H., Gebuhr, T., Bullen, P.J., Robson, S.C., Strachan, T., et al. (1997). Holt-Oram syndrome is caused by mutations in TBX5, a member of the Brachyury (T) gene family. Nat Genet *15*, 21–29. 10.1038/ng0197-21.

18. Kathiriya, I.S., Rao, K.S., Iacono, G., Devine, W.P., Blair, A.P., Hota, S.K., Lai, M.H., Garay, B.I., Thomas, R., Gong, H.Z., et al. (2021). Modeling Human TBX5 Haploinsufficiency Predicts Regulatory Networks for Congenital Heart Disease. Dev Cell *56*, 292-309.e9. 10.1016/j.devcel.2020.11.020.

19. Bruneau, B.G., Nemer, G., Schmitt, J.P., Charron, F., Robitaille, L., Caron, S., Conner, D.A., Gessler, M., Nemer, M., Seidman, C.E., et al. (2001). A murine model of Holt-Oram syndrome defines roles of the T-box transcription factor Tbx5 in cardiogenesis and disease. Cell *106*, 709–721. 10.1016/s0092-8674(01)00493-7.

20. Verzi, M.P., McCulley, D.J., Val, S.D., Dodou, E., and Black, B.L. (2005). The right ventricle, outflow tract, and ventricular septum comprise a restricted expression domain within the secondary/anterior heart field. Dev Biol *287*, 134–145. 10.1016/j.ydbio.2005.08.041.

21. Koshiba-Takeuchi, K., Mori, A.D., Kaynak, B.L., Cebra-Thomas, J., Sukonnik, T., Georges, R.O., Latham, S., Beck, L., Beck, L., Henkelman, R.M., et al. (2009). Reptilian heart development and the molecular basis of cardiac chamber evolution. Nature *461*, 95–98. 10.1038/nature08324.

22. Xie, L., Hoffmann, A.D., Burnicka-Turek, O., Friedland-Little, J.M., Zhang, K., and Moskowitz, I.P. (2012). Tbx5-Hedgehog Molecular Networks Are Essential in the Second Heart Field for Atrial Septation. Dev Cell *23*, 280–291. 10.1016/j.devcel.2012.06.006.

23. Mori, A.D., and Bruneau, B.G. (2004). TBX5 mutations and congenital heart disease: Holt-Oram syndrome revealed. Curr Opin Cardiol *19*, 211–215.

24. Mommersteeg, M.T.M., Yeh, M.L., Parnavelas, J.G., and Andrews, W.D. (2015). Disrupted Slit-Robo signalling results in membranous ventricular septum defects and bicuspid aortic valves. Cardiovasc Res *106*, 55–66. 10.1093/cvr/cvv040.

25. Li, Y., Klena, N.T., Gabriel, G.C., Liu, X., Kim, A.J., Lemke, K., Chen, Y., Chatterjee, B., Devine, W., Damerla, R.R., et al. (2015). Global genetic analysis in mice unveils central role for cilia in congenital heart disease. Nature *521*, 1–16. 10.1038/nature14269.

26. Kruszka, P., Tanpaiboon, P., Neas, K., Crosby, K., Berger, S.I., Martinez, A.F., Addissie, Y.A., Pongprot, Y., Sittiwangkul, R., Silvilairat, S., et al. (2017). Loss of function in ROBO1 is associated with tetralogy of Fallot and septal defects. J Med Genet *54*, 825. 10.1136/jmedgenet-2017-104611.

27. Larrieu-Lahargue, F., Thomas, K.R., and Li, D.Y. (2012). Netrin Ligands and Receptors: Lessons From Neurons to the Endothelium. Trends Cardiovas Med *22*, 44–47. 10.1016/j.tcm.2012.06.010.

28. Akerberg, B.N., Gu, F., VanDusen, N.J., Zhang, X., Dong, R., Li, K., Zhang, B., Zhou, B., Sethi, I., Ma, Q., et al. (2019). A reference map of murine cardiac transcription factor chromatin occupancy identifies dynamic and conserved enhancers. Nat Commun *10*, 4907. 10.1038/s41467-019-12812-3.

29. Bin, J.M., Han, D., Sun, K.L.W., Croteau, L.-P., Dumontier, E., Cloutier, J.-F., Kania, A., and Kennedy, T.E. (2015). Complete Loss of Netrin-1 Results in Embryonic Lethality and Severe Axon Guidance Defects without Increased Neural Cell Death. CellReports *12*, 1099–1106. 10.1016/j.celrep.2015.07.028.

30. Lewandoski, M., Meyers, E.N., and Martin, G.R. (1997). Analysis of Fgf8 gene function in vertebrate development. Cold Spring Harb Sym *62*, 159–168.

31. Kiemen, A.L., Braxton, A.M., Grahn, M.P., Han, K.S., Babu, J.M., Reichel, R., Jiang, A.C., Kim, B., Hsu, J., Amoa, F., et al. (2022). CODA: quantitative 3D reconstruction of large tissues at cellular resolution. Nat Methods, 1–10. 10.1038/s41592-022-01650-9.

32. VanDusen, N.J., Casanovas, J., Vincentz, J.W., Firulli, B.A., Osterwalder, M., Lopez-Rios, J., Zeller, R., Zhou, B., Grego-Bessa, J., De La Pompa, J.L., et al. (2014). Hand2 Is an Essential Regulator for Two Notch-Dependent Functions within the Embryonic Endocardium. Cell Rep. *9*, 2071–2083. 10.1016/j.celrep.2014.11.021.

33. George, R.M., Firulli, B.A., Podicheti, R., Rusch, D.B., Mannion, B.J., Pennacchio, L.A., Osterwalder, M., and Firulli, A.B. (2023). Single cell evaluation of endocardial HAND2 gene regulatory networks reveals critical HAND2 dependent pathways impacting cardiac morphogenesis. Development *150*. 10.1242/dev.201341.

34. Bin, J.M., Han, D., Lai Wing Sun, K., Croteau, L.-P., Dumontier, E., Cloutier, J.-F., Kania, A., and Kennedy, T.E. (2015). Complete Loss of Netrin-1 Results in Embryonic Lethality and

Severe Axon Guidance Defects without Increased Neural Cell Death. Cell Reports *12*, 1099–1106. 10.1016/j.celrep.2015.07.028.

35. Tasic, B., Hippenmeyer, S., Wang, C., Gamboa, M., Zong, H., Chen-Tsai, Y., and Luo, L. (2011). Site-specific integrase-mediated transgenesis in mice via pronuclear injection. Proc National Acad Sci *108*, 7902–7907. 10.1073/pnas.1019507108.

36. Madisen, L., Zwingman, T.A., Sunkin, S.M., Oh, S.W., Zariwala, H.A., Gu, H., Ng, L.L., Palmiter, R.D., Hawrylycz, M.J., Jones, A.R., et al. (2010). A robust and high-throughput Cre reporting and characterization system for the whole mouse brain. Nat Neurosci *13*, 133–140. 10.1038/nn.2467.

37. Dominguez, M.H., Krup, A.L., Muncie, J.M., and Bruneau, B.G. (2023). Graded mesoderm assembly governs cell fate and morphogenesis of the early mammalian heart. Cell *186*, 479-496.e23. 10.1016/j.cell.2023.01.001.

38. Schindelin, J., Arganda-Carreras, I., Frise, E., Kaynig, V., Longair, M., Pietzsch, T., Preibisch, S., Rueden, C., Saalfeld, S., Schmid, B., et al. (2012). Fiji: an open-source platform for biological-image analysis. Nat. Methods *9*, 676–682. 10.1038/nmeth.2019.

39. Kirshner, H., Aguet, F., Sage, D., and Unser, M. (2013). 3-D PSF fitting for fluorescence microscopy: implementation and localization application. J. Microsc. *249*, 13–25. 10.1111/j.1365-2818.2012.03675.x.

40. Hörl, D., Rusak, F.R., Preusser, F., Tillberg, P., Randel, N., Chhetri, R.K., Cardona, A., Keller, P.J., Harz, H., Leonhardt, H., et al. (2019). BigStitcher: reconstructing high-resolution image datasets of cleared and expanded samples. Nat Methods *16*, 870–874. 10.1038/s41592-019-0501-0.

41. Tinevez, J.-Y., Perry, N., Schindelin, J., Hoopes, G.M., Reynolds, G.D., Laplantine, E., Bednarek, S.Y., Shorte, S.L., and Eliceiri, K.W. (2017). TrackMate: An open and extensible platform for single-particle tracking. Methods *115*, 80–90. 10.1016/j.ymeth.2016.09.016.

42. Satija, R., Farrell, J.A., Gennert, D., Schier, A.F., and Regev, A. (2015). Spatial reconstruction of single-cell gene expression data. Nat Biotechnol *33*, 495–502. 10.1038/nbt.3192.

43. Butler, A., Hoffman, P., Smibert, P., Papalexi, E., and Satija, R. (2018). Integrating single-cell transcriptomic data across different conditions, technologies, and species. Nat Biotechnol *48*, 1070–17. 10.1038/nbt.4096.

44. Stuart, T., Butler, A., Hoffman, P., Hafemeister, C., Papalexi, E., III, W.M.M., Hao, Y., Stoeckius, M., Smibert, P., and Satija, R. (2019). Comprehensive Integration of Single-Cell Data. Cell *177*, 1–37. 10.1016/j.cell.2019.05.031.

45. Becht, E., McInnes, L., Healy, J., Dutertre, C.-A., Kwok, I.W.H., Ng, L.G., Ginhoux, F., and Newell, E.W. (2018). Dimensionality reduction for visualizing single-cell data using UMAP. Nat Biotechnol. 10.1038/nbt.4314.

46. Forjaz, A., Vaz, E., Romero, V.M., Joshi, S., Braxton, A.M., Jiang, A.C., Fujikura, K., Cornish, T., Hong, S.-M., Hruban, R.H., et al. (2023). Three-dimensional assessments are necessary to determine the true spatial tissue composition of diseased tissues. bioRxiv, 2023.12.04.569986. 10.1101/2023.12.04.569986.

Acknowledgements. We thank Brian Black for mouse lines and members of the Bruneau lab for troubleshooting help, discussions and comments. We also thank the Gladstone Bioinformatics, Genomics, and Histology and Microscopy Cores, the UCSF Laboratory for Cell Analysis, and the UCSF Center for Advanced Technology. This work was supported by grants from the National Institutes of Health (NHLBI Bench to Bassinet Program UM1HL098179 to B.G.B.; R01HL114948 to B.G.B., R01HL155906 to B.G.B. and I.S.K., U54CA268083 and UG3CA275681 to A.L.K.), Additional Ventures to B.G.B., Society for Pediatric Anesthesia (Young Investigator Award to I.S.K.), Hellman Family Fund (I.S.K.), UCSF REAC Grant (I.S.K.), UCSF Pediatric Heart Center Catalyst Award to I.S.K. and UCSF Department of Anesthesia and Perioperative Care (Ongoing Investigator Award to I.S.K.). This work was also supported by an NIH/NCRR grant (C06 RR018928) to the J. David Gladstone Institutes, and the Younger Family Fund (B.G.B.).

Author Contributions. W.P.D. and B.G.B. originally conceived, and I.S.K. and B.G.B. refined and developed the study. W.P.D. made initial observations using genetic lineage tools that he gathered or generated, such as *ROSA26*^{Ai66b} and the intersectional-*DTA*. I.S.K., M.H.D., W.P.D. and K.M.H. performed embryo dissections. K.M.H., B.I.G., P.G., M.N.M., T.S., D.M.P., S.W. and E.F.B. managed animal husbandry and genotyping. I.S.K., M.H.D., W.P.D. and K.M.H. performed whole mount or section immunostaining experiments and imaging. M.H.D., J.M.M. and D.Q performed lightsheet imaging and processing, and M.H.D. and J.M.M. implemented analyses with hypothesis-based input from I.S.K. I.S.K. designed strategy to use 5’ sequencing kit and developed synthetic genome with Gladstone Bioinformatics core, micro-dissected heart regions for scRNA-seq and processed samples with K.S.R. and P.G. for sequencing library

preparations. K.S.R. generated scRNA-seq libraries and performed scRNA-seq analyses with hypothesis-based input from I.S.K. K.S.R., K.M.H., P.G. and M.N.M. performed section *in situ* hybridization and imaging. K.S.R. generated ChIP-seq browser tracks with input from S.H. I.S.K. assessed cardiac defects by histology and provided anatomical knowledge to A.L.K. to apply a deep learning tool for cardiac morphometry. A.F. trained deep learning models and was supervised by A.L.K. and advised by P-H.W. and D.W. B.G.B. supervised and advised the study. I.S.K. and K.S.R. prepared figures. I.S.K. wrote the original draft with contributions from co-authors. I.S.K. and B.G.B. reviewed and edited the manuscript with input from co-authors.

Declaration of Interests: B.G.B. is a co-founder and shareholder of Tenaya Therapeutics. B.G.B. is an advisor for Silver Creek Pharmaceuticals. None of the work presented here is related to these commercial interests.

Figure 1

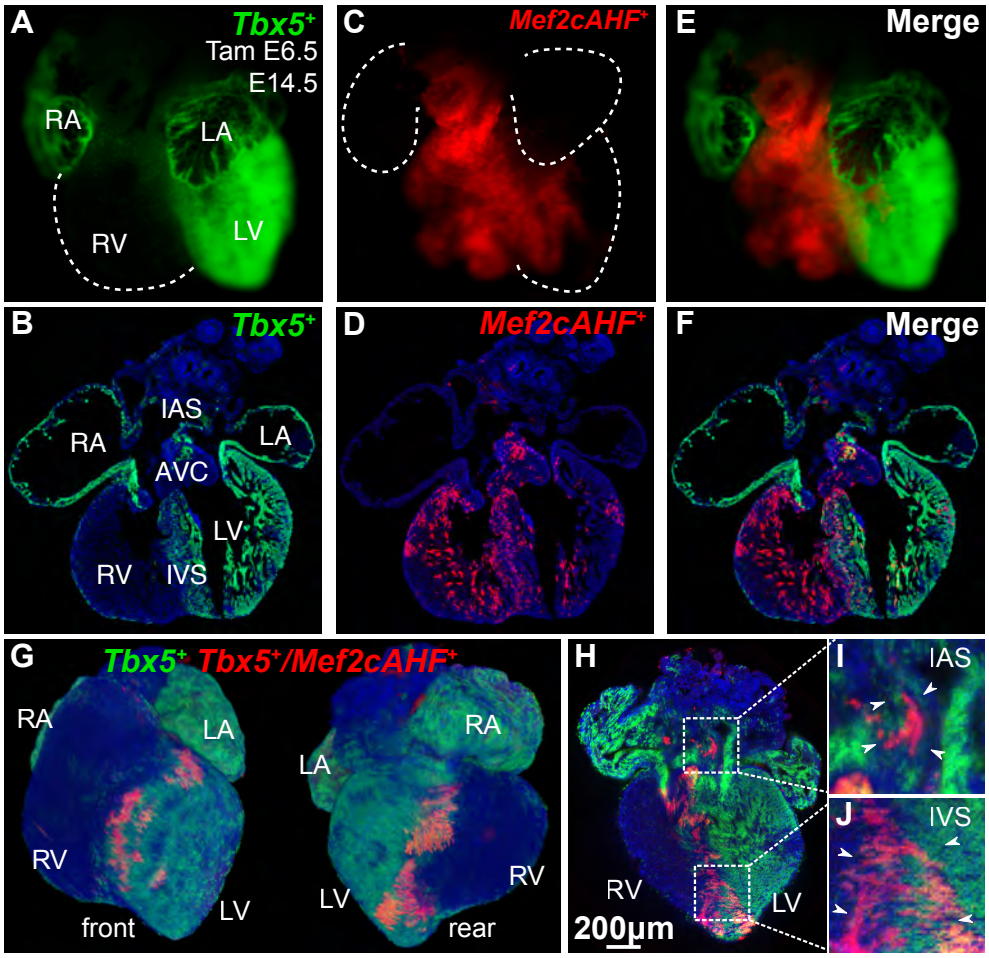

Figure 1. *Tbx5*$^{+}$/*Mef2cAHF*$^{+}$ lineage marks a compartment boundary at the cardiac interventricular septum At E14.5, (A, B) clonal cell descendants of a *Tbx5*$^{+}$ lineage (ZsGreen) labeled at E6.5 contributes to the LV, and (C, D) a *Mef2cAHF*$^{+}$ lineage (tdTomato immunostaining) contributes to the RV, demonstrating largely complementary patterns. (F-J) These lineages overlap (*Tbx5*$^{+}$/*Mef2cAHF*$^{+}$) at the interventricular septum (IVS), as well as the atrioventricular canal (AVC) and interatrial septum (IAS). *Tbx5*$^{CreERT2/+}$; *Mef2cAHF-DreERT2*; *Rosa26*$^{Ai6/Ai66b}$ hearts by epifluorescence microscopy (A-C) and cryosections (D-F). (G-J) Maximal projection images by light sheet microscopy of an intersectional reporter for the *Tbx5*$^{+}$/*Mef2cAHF*$^{+}$ lineage (tdTomato immunostaining) in *Tbx5*$^{CreERT2/+}$; *Mef2cAHF-DreERT2*; *Rosa26*$^{Ai66/+}$ embryos.

Figure S1

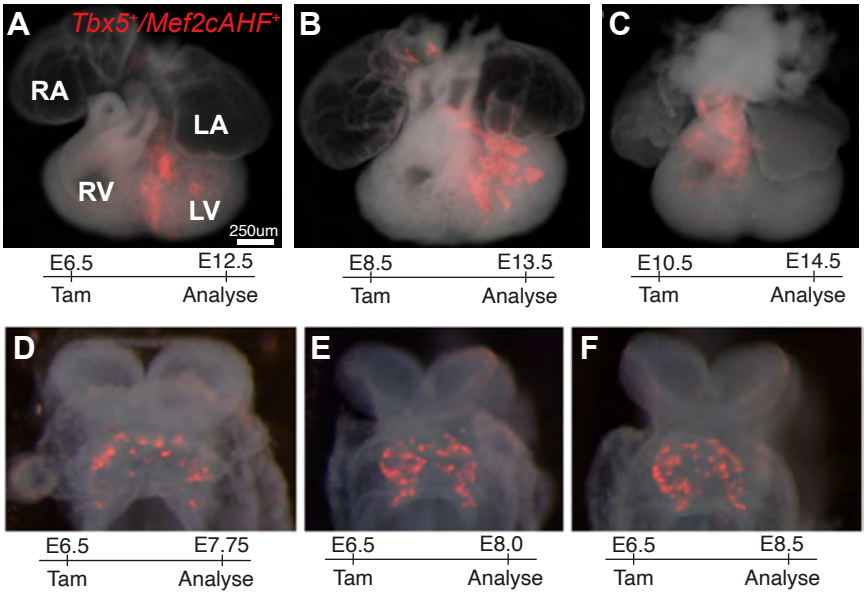

Supplemental Figure 1. (A-C) *Tbx5*$^{+}$*/Mef2cAHF*$^{+}$ lineage contributions to the interventricular septum were descendants from progenitors labeled at (A) E6.5, but not at (B) E8.5 or (C) E10.5 in *Tbx5*$^{CreERT2/+}$; *Mef2cAHF-DreERT2*; *Rosa26*$^{Ai6/Ai66}$ embryos. Epifluorescence microscopy images of the *Tbx5*$^{+}$*/Mef2cAHF*$^{+}$ lineage (tdTomato immunostaining) labeled at E6.5 from (A) E7.75, (B) E8.0 and (C) E8.5 displayed an apparent “salt and pepper” pattern in the early developing heart.

Figure 2

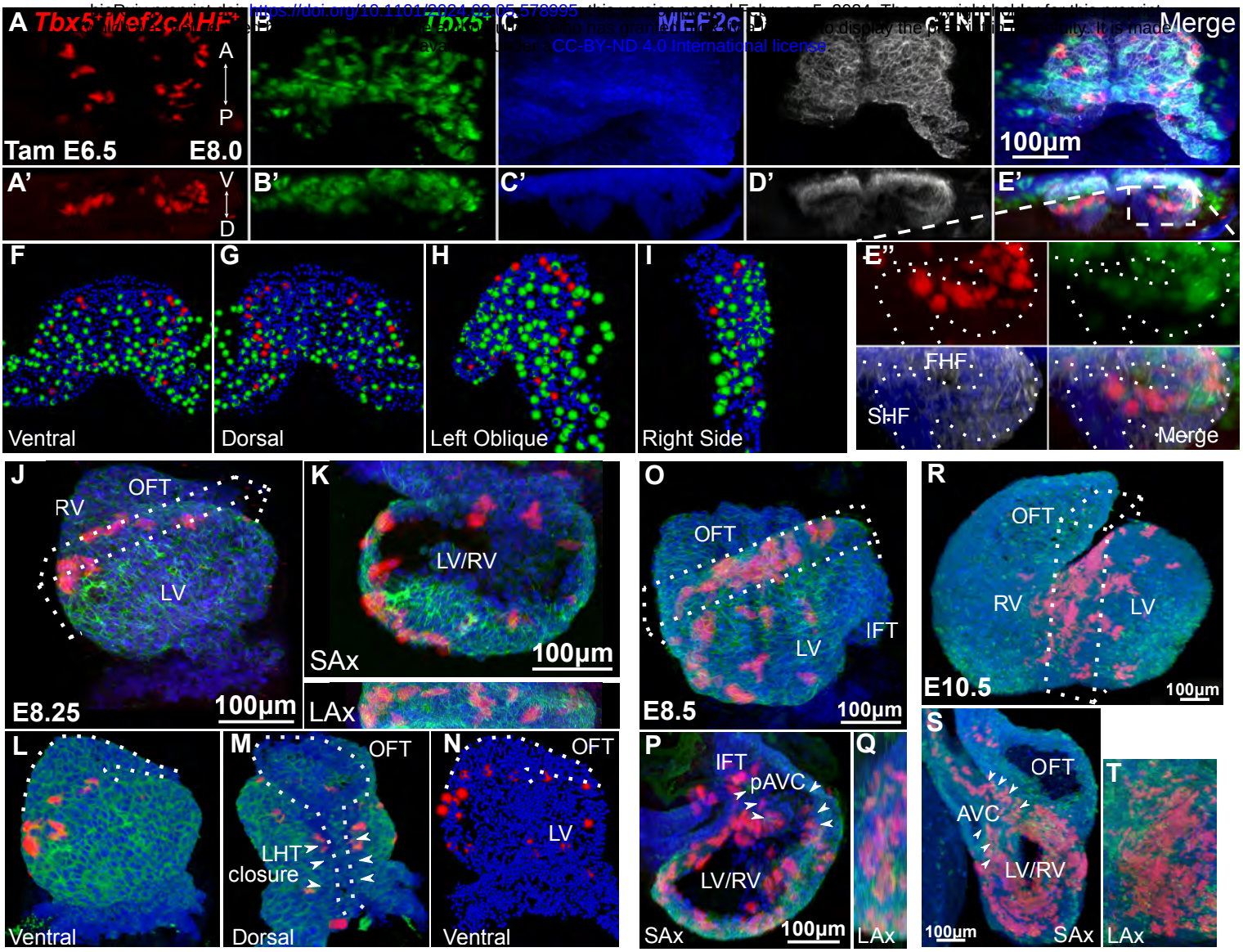

Figure 2. *Tbx5*$^{+}$*/Mef2cAHF*$^{+}$ lineage is prefigured in early mouse heart development. Frontal (A-E), transverse (A'-E') and magnified transverse (E'') views of maximum Z-projections of whole mount embryos by lightsheet imaging at E8.0 show the *Tbx5*$^{+}$ lineage (ZsGreen), and immunostaining of tdTomato for the *Tbx5*$^{+}$*/Mef2cAHF*$^{+}$ lineage, MEF2c and cTNT in *Tbx5*$^{CreERT2/+}$; *Mef2cAHF-DreERT2*; *Rosa26*$^{Ai6/Ai66}$ embryos. A-P, anterior-posterior axis; V-D, ventral-dorsal axis. First (FHF) and second (SHF) heart fields. At E8.0 (approximately 3 somites), *Tbx5*$^{+}$ lineage cells are restricted to a ventral domain corresponding to the FHF, whereas *Tbx5*$^{+}$*/Mef2cAHF*$^{+}$ lineage cells originate along the FHF-SHF boundary. *Tbx5*$^{+}$*/Mef2cAHF*$^{+}$ lineage cells lie in an apparent planar ringlet in the dorsal-ventral axis that expands as the heart tube grows. (J-N) At E8.25 (approximately 6 somites), with dorsal closure of the linear heart tube (LHT) underway, the *Tbx5*$^{+}$*/Mef2cAHF*$^{+}$ lineage cells form a ring situated between the RV and LV primordia, which is observed from multiple perspectives including anterior, short-axis (SAx) and long-axis (LAx) views. (O-Q) At E8.5 (approximately 9 somites), *Tbx5*$^{+}$*/Mef2cAHF*$^{+}$ lineage cells are observed in a portion of the AVC primoridium (pAVC and arrowheads). (R-T) At E10.5, a band of *Tbx5*$^{+}$*/Mef2cAHF*$^{+}$ lineage cells extends from the interventricular groove at the outer curvature to the inner curvature of the heart. SAx and LAx show that *Tbx5*$^{+}$*/Mef2cAHF*$^{+}$ lineage cells occupies a crossroads for heart morphogenesis, spanning the growing interventricular septum to the AVC, adjacent to the OFT.

Figure S2

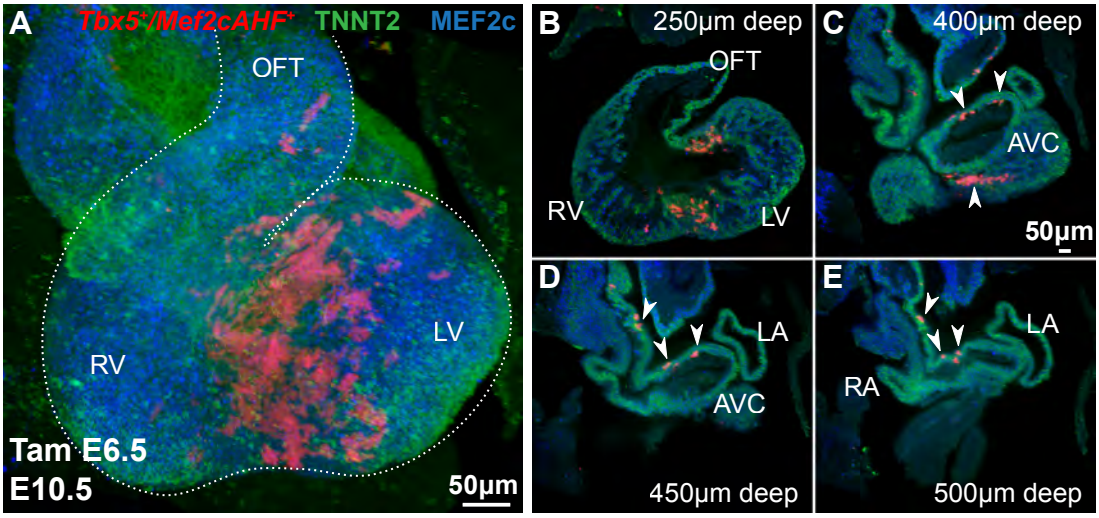

Supplemental Figure 2. (A-E) In the developing atria, optical sections from ventral to dorsal show lineage-labeled *Tbx5*$^{+}$/*Mef2cAHF*$^{+}$ lineage cells from the AV cushion (AVC) region to the roof of the atrium, prior to the formation of the interatrial septum, in *Tbx5*$^{CreERT2/+}$; *Mef2cAHF-DreERT2*; *Rosa26*$^{Ai6/Ai66}$ embryos.

Figure 3

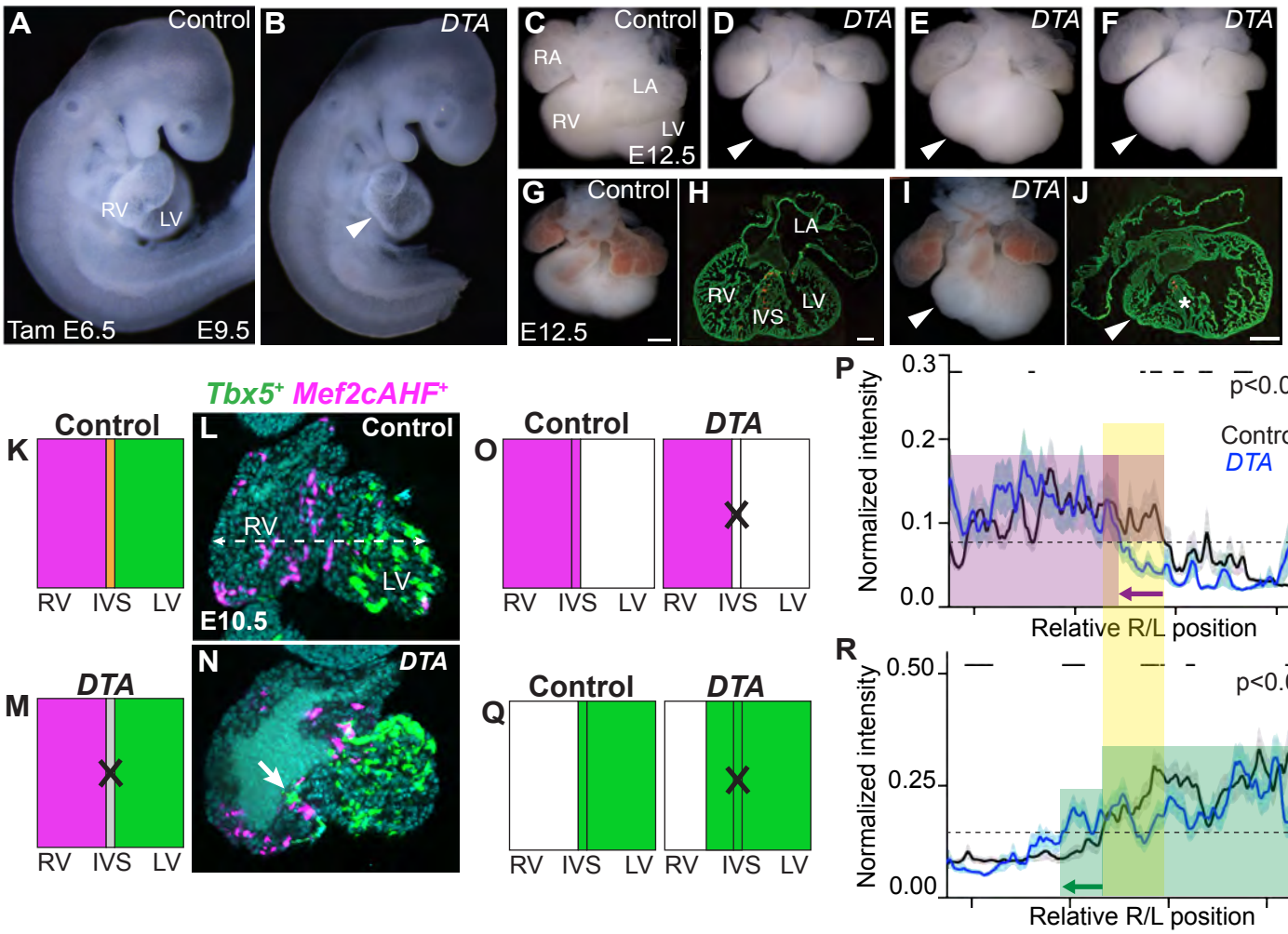

Figure 3. Cell ablation of *Tbx5*$^{+}$/*Mef2cAHF*$^{+}$ progenitors causes RV hypoplasia, IVS disorganization, and lineage mixing. Misexpression of *diphtheria toxin* (*DTA*) in *Tbx5*$^{+}$/*Mef2cAHF*$^{+}$ progenitors in *Tbx5*$^{CreERT2/+}$; *Mef2cAHF-DreERT2*; *Rosa26*$^{Ai66/+}$; *Hip11*$^{intersectional-DTA/+}$ embryos (*DTA*), compared to *Tbx5*$^{CreERT2/+}$; *Mef2cAHF-DreERT2*; *Rosa26*$^{Ai66/+}$; *Hip11*$^{+/+}$ (control), resulted in RV hypoplasia (arrows) at E9.5 (A, B), and E12.5 (C-J), along with disorganization and non-compaction of the interventricular septum (IVS) (asterisk) (G-J). (K-N) At E10.5, mixing of the *Mef2cAHF*$^{+}$ lineage and *Tbx5*$^{+}$ lineage (white arrow in N shows ectopic *Tbx5*$^{+}$ lineage ZsGreen cell in the right heart) was observed by lightsheet microscopy in *Tbx5*$^{CreERT2/+}$; *Mef2cAHF-DreERT2*; *Rosa26*$^{Ai6/Ai66b}$; *Hip11*$^{intersectional-DTA/+}$ embryos (*DTA*) (n=2) compared to *Tbx5*$^{CreERT2/+}$; *Mef2cAHF-DreERT2*; *Rosa26*$^{Ai6/Ai66b}$; *Hip11*$^{+/+}$ embryos (control) (n=2). (O-R) Linear profiles quantified fluorescence intensity above a threshold (dashed line in P,R) across the heart at the right or left (R/L) positions. *Mef2cAHF*$^{+}$ lineage retreated rightward (depiction in O, purple arrow in P) while *Tbx5*$^{+}$ lineage cells expanded rightward into the RV (depiction in Q, green arrow in R), consistent with a compartment boundary disruption. Yellow shading represents *Tbx5*$^{+}$/*Mef2cAHF*$^{+}$ lineage cells and region of cell ablation. Statistical significance ($p<0.05$) between control and *DTA* mutants was determined by Welch's two-sample t-test at each position along the right-left axis.

Figure S3

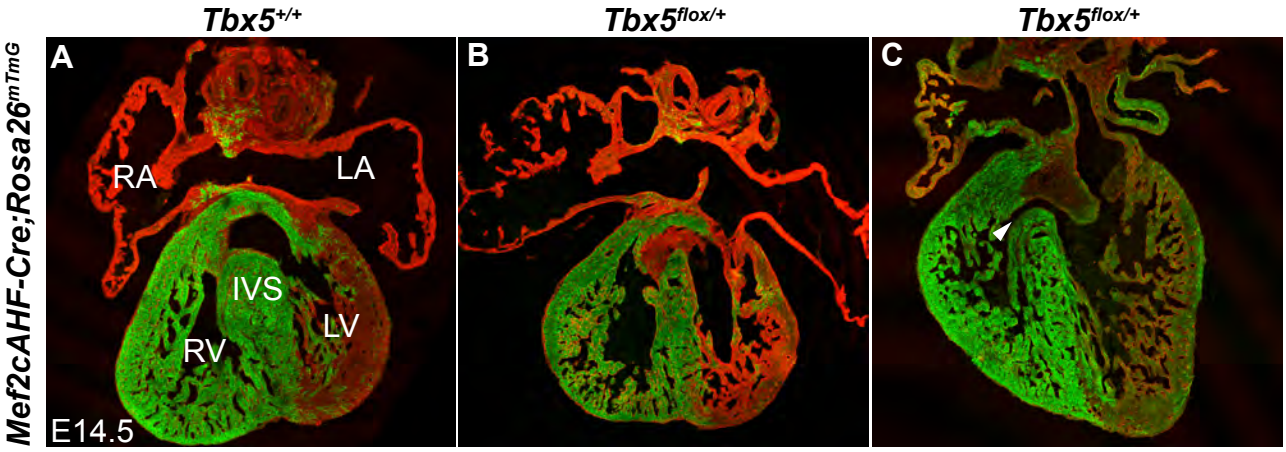

Supplemental Figure 3. Conditional haploinsufficiency of *Tbx5* in the interventricular septum (IVS) leads to ventricular septal defects (VSDs). (A-C) At E14.5, membranous VSDs were observed in *Mef2cAHF-Cre*;*ROSA26*$^{mTmG/+}$;*Tbx5*$^{flox/+}$ mutant embryos (n=4/7) compared to *Mef2cAHF-Cre*;*ROSA26*$^{mTmG/+}$;*Tbx5*$^{flox/+}$ controls (n=0/3).

Figure 4

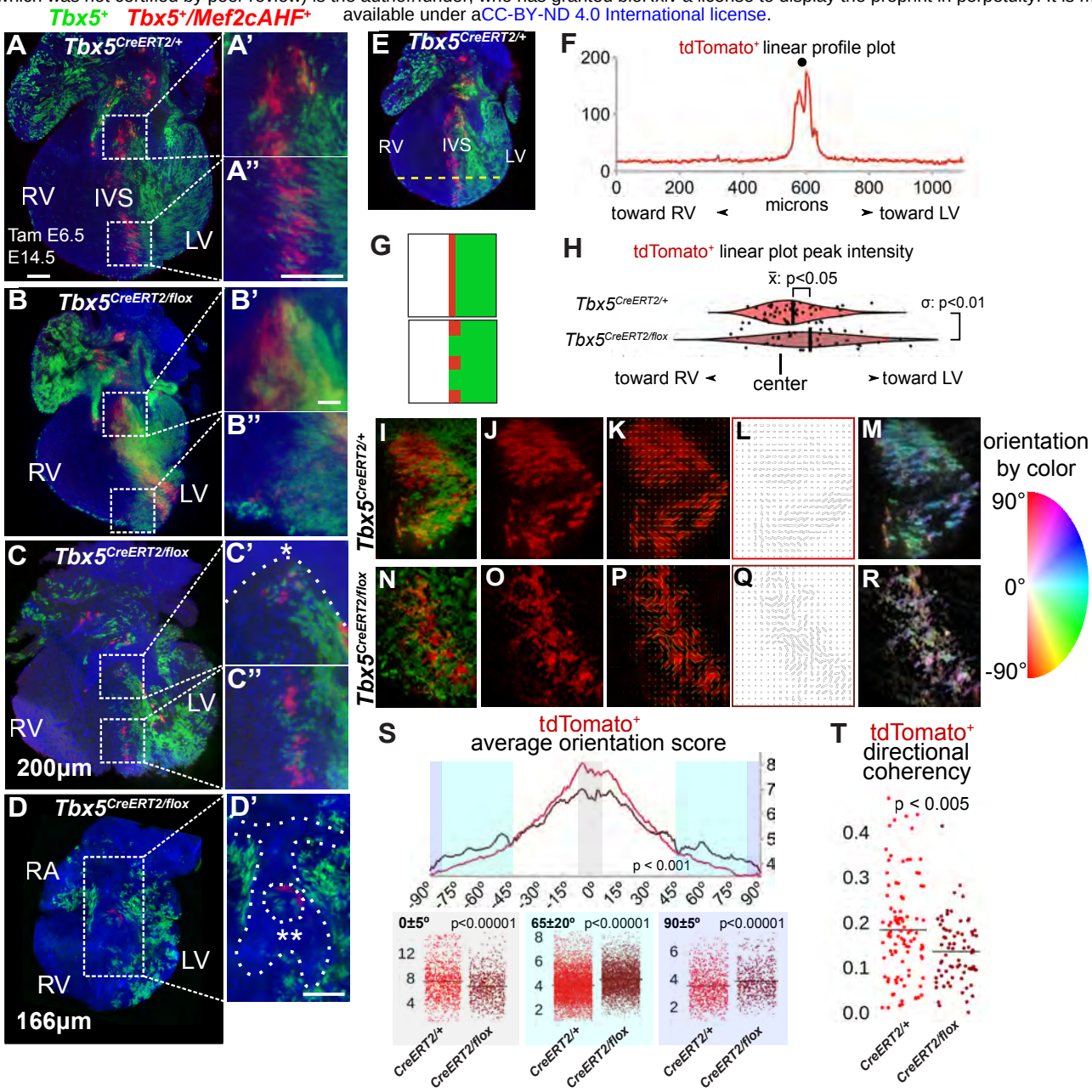

Figure 4. Reduced Tbx5 dosage caused ventricular septal defects and perturbations to IVS boundary position and integrity. (A) Mid-posterior optical sections from light sheet microscopy of a control (*Tbx5*$^{CreERT2/+}$;*Mef2cAHF-DreERT2*;*ROSA26*$^{Ai6/Ai66}$) heart display *Tbx5*$^{+}$ lineage (ZsGreen) and *Tbx5*$^{+}$/*Mef2cAHF*$^{+}$ lineage (tdTomato immunostaining) cells. *Tbx5*$^{+}$/*Mef2cAHF*$^{+}$ lineage cells in the interventricular septum (IVS) extended from the base (A') to the apex (A") of the heart, where cells were highly organized. (B-D) A spectrum of phenotypes of *Tbx5*$^{CreERT2/flox}$ mutants (*Tbx5*$^{CreERT2/flox}$;*Mef2cAHF-DreERT2*;*ROSA26*$^{Ai6/Ai66}$) were observed, including intact IVS (B-B"), membranous VSD (C-C", asterisk) and atrioventricular septal defect (double asterisk in D'). (B', B", C', C", D') A reduction, maldistribution and disorientation of *Tbx5*$^{+}$/*Mef2cAHF*$^{+}$ lineage cells were observed in *Tbx5*$^{CreERT2/flox}$ mutants. (E-H) Linear plot profiles at positions along the anterior-posterior and apical-basal axis of control (n=4) and *Tbx5*$^{CreERT2/flox}$ mutant (n=3) hearts for *Tbx5*$^{+}$/*Mef2cAHF*$^{+}$ lineage cells showed a leftward shift of boundary positioning and broadening of the *Tbx5*$^{+}$/*Mef2cAHF*$^{+}$ lineage position, consistent with lineage mixing. (E,F) An example of a linear profile plot is shown, and (G,H) aggregated data is depicted and quantified. (I-T) Orientation scores for cells from each channel (tdTomato^{+} or ZsGreen^{+}) was delineated for each genotype, and distributions were plotted as a function of angle. *Tbx5*$^{CreERT2/flox}$ mutant hearts scored worse for orientation of *Tbx5*$^{+}$/*Mef2cAHF*$^{+}$ lineage (tdTomato^{+}) cells in the dominant direction (range from -5 to 5 degrees) and scored higher in the orientation orthogonal to the dominant direction (range from 85 to 95 degrees and -85 to -95 degrees), as determined (S) by Watson's two-sample test across all orientations or by Wilcoxon signed-rank test for selected orientations. (T) *Tbx5*$^{+}$/*Mef2cAHF*$^{+}$ lineage (tdTomato^{+}) cells demonstrated worse directional coherency scoring in *Tbx5*$^{CreERT2/flox}$ mutants by Wilcoxon signed-rank test.

Figure S4

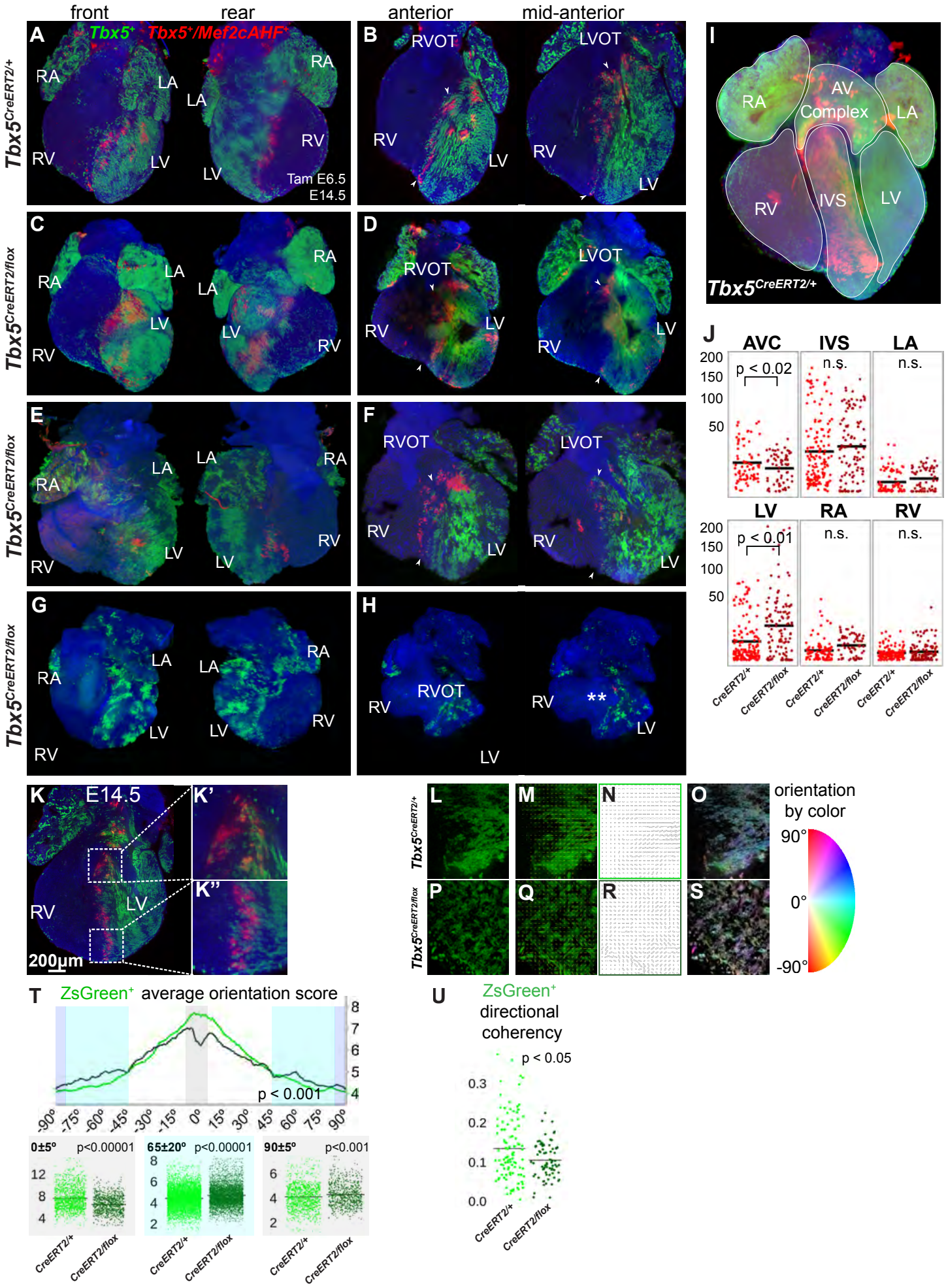

Supplemental Figure 4. (A-H) Volume renderings from lightsheet microscopy of anterior and posterior surfaces, as well as anterior and mid-anterior 4-chamber optical sections of *Tbx5*$^{CreERT2/+}$ control (*Tbx5*$^{CreERT2/+}$;*Mef2cAHF-DreERT2*;*ROSA26*$^{Ai6/Ai66}$) and *Tbx5*$^{CreERT2/flox}$ mutant (*Tbx5*$^{CreERT2/flox}$;*Mef2cAHF-DreERT2*;*ROSA26*$^{Ai6/Ai66}$) hearts at E14.5 display *Tbx5*$^{+}$ lineage (ZsGreen) and *Tbx5*$^{+}$/*Mef2cAHF*$^{+}$ lineage (tdTomato immunostaining) cells. (I, J) Quantification of the anatomical location of tdTomato^{+} and ZsGreen^{+} cells in *Tbx5*$^{CreERT2/flox}$ mutants (n=4) and *Tbx5*$^{CreERT2/+}$ controls (n=4), by region as outlined in (I). Over 1200 3-dimensional regions of interest were drawn blinded, and then integrated fluorescence signal was assessed. (J) Although no regional differences in the intensities of ZsGreen^{+} were detected, tdTomato^{+} displayed higher integrated fluorescence in the left ventricle (LV) and less signal in atrioventricular canal (AVC) by Wilcoxon signed-rank test. (L-U) *Tbx5*$^{CreERT2/flox}$ mutant hearts scored worse for orientation scores of *Tbx5*$^{+}$ lineage (ZsGreen^{+}) cells in the dominant direction (range from -5 to 5 degrees) and scored higher in the orientation orthogonal to the dominant direction (range from 85 to 95 degrees and -85 to -95 degrees), as determined (T) by Watson's two-sample test across all orientations or by Wilcoxon signed-rank test for selected orientations. (U) *Tbx5*$^{+}$ lineage (ZsGreen^{+}) cells demonstrated worse directional coherency scoring in *Tbx5*$^{CreERT2/flox}$ mutants by Wilcoxon signed-rank test.

Figure 5

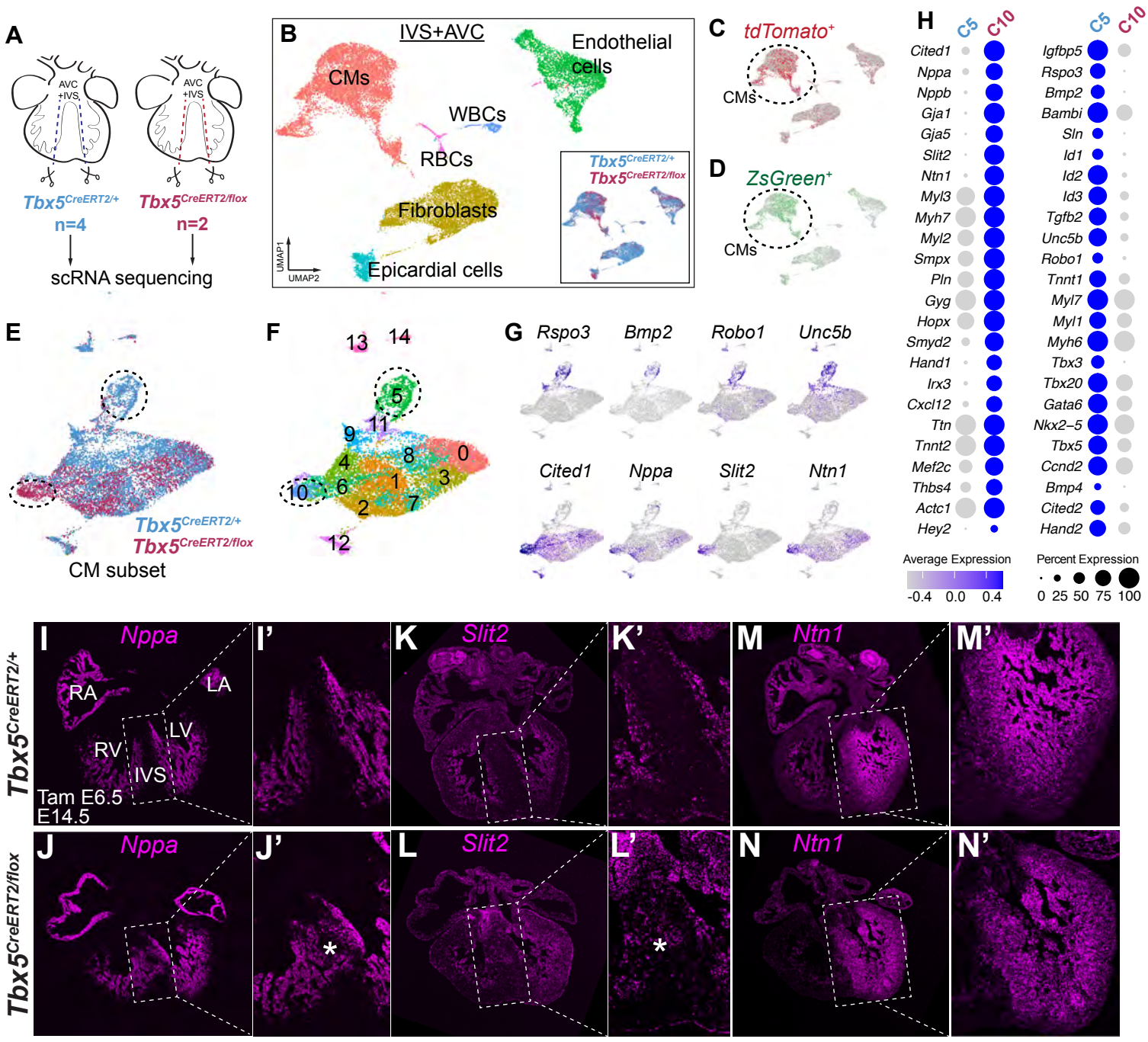

Figure 5. *Slit2* and *Ntn1* are *Tbx5*-sensitive genes in the interventricular septum (IVS). (A) At E13.5, we micro-dissected the right ventricle (RV), left ventricle (LV) and IVS+atrioventricular canal (AVC) in *Tbx5*$^{CreERT2/+}$ controls (*Tbx5*$^{CreERT2/+}$;*Mef2cAHF-DreERT2*;*ROSA26*$^{Ai6/Ai66}$)(n=4) and *Tbx5*$^{CreERT/flox}$ mutants (*Tbx5*$^{CreERT2/flox}$*;Mef2cAHF-DreERT2*;*ROSA26*$^{Ai6/Ai66}$)(n=2) with the labeled *Tbx5*$^{+}$*/Mef2cAHF*$^{+}$ lineage (*tdTomato*$^{+}$) and *Tbx5*$^{+}$ lineage (*ZsGreen*$^{+}$) cells, after tamoxifen at E6.5. (B) UMAP visualization by cell type clusters and *Tbx5* genotype (inset). CMs, cardiomyocytes; WBCs, white blood cells; RBCs, red blood cells. (C) *ZsGreen*$^{+}$ and (D) *tdTomato*$^{+}$ cells are enriched among CMs. (E) UMAP shows a *Tnnt2*$^{+}$ CM subset by *Tbx5* genotype or (F) Louvain clusters. (G) Feature plots show that atrioventricular canal genes (*Rspo3, Bmp2, Robo1, Unc5b*) are enriched among control-enriched cluster 5, suggesting downregulation of these genes in *Tbx5* mutants. Trabecular genes (*Cited1, Nppa, Slit2, Ntn1*) were enriched in the *Tbx5* mutant-enriched cluster 10. (H) Dot plots of selected genes that are upregulated in cluster 10 (C10) or in cluster 5 (C5). Significance of adj $p<0.05$ was determined by Wilcoxan rank sum. (I-N) Fluorescent *in situ* hybridization of trabecular genes *Nppa*, *Slit2* and *Ntn1* in *Tbx5*$^{CreERT2/+}$ controls or *Tbx5*$^{CreERT2/flox}$ mutants at E14.5. (I, K) *Nppa* and *Slit2* are normally expressed in the ventricular trabecular layer and excluded from the core of the IVS. (J, L) In a *Tbx5*$^{CreERT2/flox}$ mutant with an intact IVS, *Nppa* and *Slit2* are misexpressed in the IVS (asterisk). (M) *Ntn1* is normally expressed in the trabecular layer and in a gradient across the IVS, from left to right. (N) In a *Tbx5*$^{CreERT2/flox}$ mutant with an intact IVS, *Ntn1* is expanded across the IVS, flattening its gradient.

Figure S5

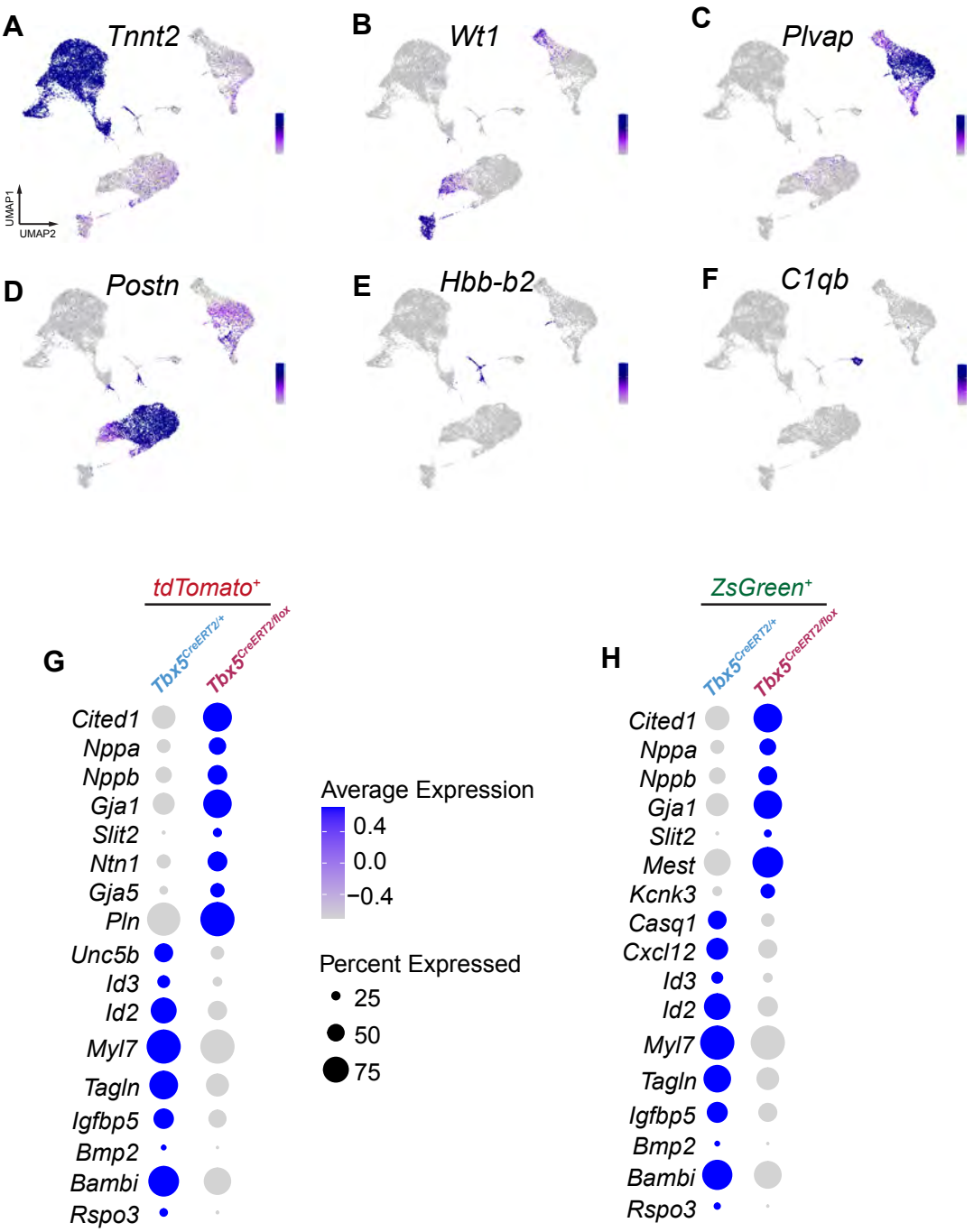

Supplemental Figure 5. In scRNA-seq samples from the IVS+AVC region, we detected clusters enriched for (A) *Tnnt2*$^{+}$ cardiomyocytes (CMs), (B) *Tbx18*$^{+}$*/Wt1*$^{+}$ epicardial cells, (C) *Plvap*$^{+}$ endothelial cells, (D) *Postn*$^{+}$ fibroblasts, (E) *Hbb-b2*$^{+}$ red blood cells, and (F) *C1qb*$^{+}$ white blood cells. Dot plots of selected differentially expressed genes in (G) *tdTomato*$^{+}$ or (H) *ZsGreen*$^{+}$ cells. Significance of adj $p<0.05$ was determined by Wilcoxan rank sum.

Figure S6

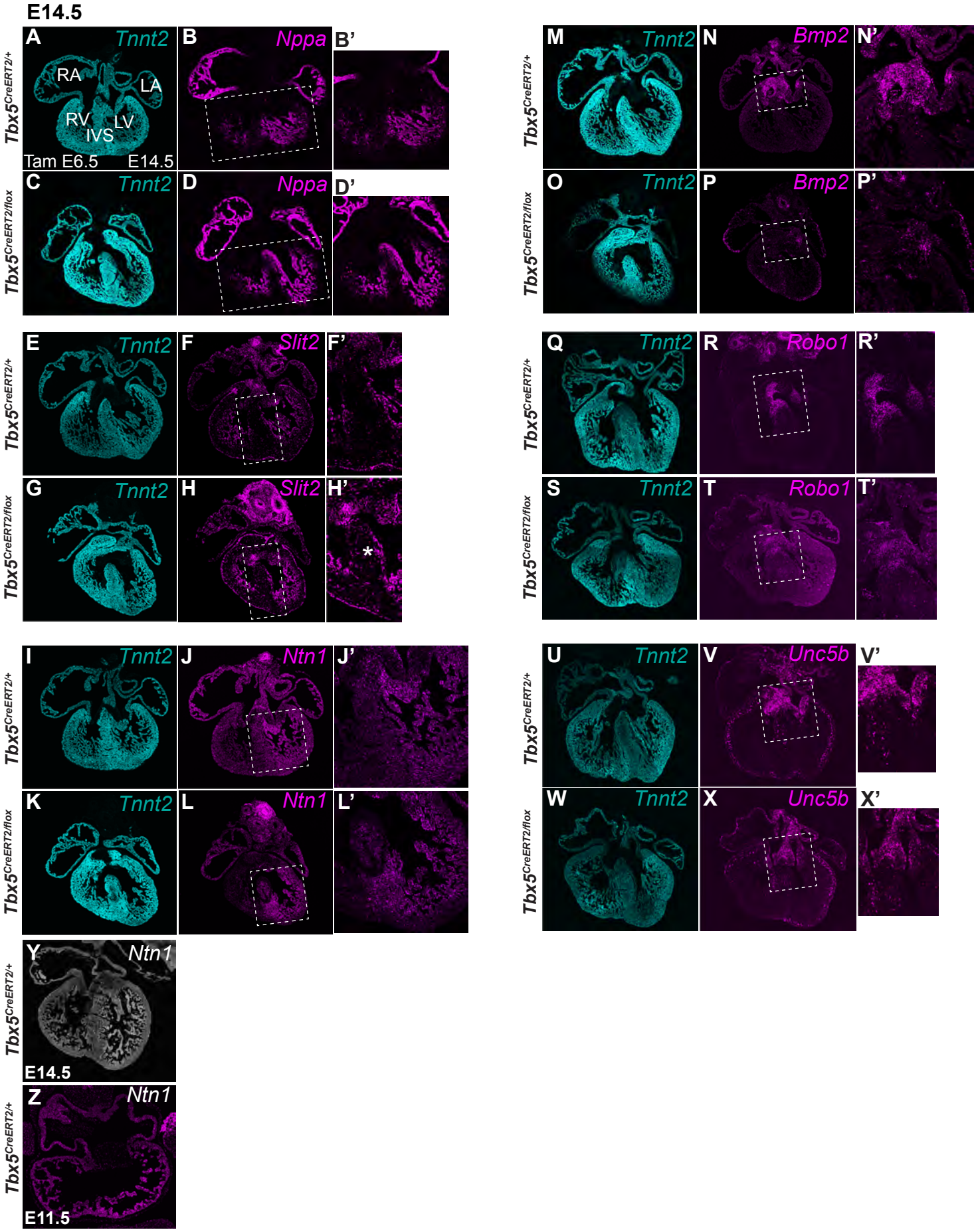

Supplemental Figure 6. Fluorescent *in situ* hybridization of *Tbx5*-dependent genes. (A-L') Fluorescent *in situ* hybridization at E14.5 after tamoxifen at E6.5 of *Nppa*, *Slit2* and *Ntn1* are expressed in the trabecular layer in *Tbx5*$^{CreERT2/+}$ controls (*Tbx5*$^{CreERT2/+}$;*Mef2cAHF-DreERT2*;*ROSA26*$^{Ai6/Ai66}$), and misexpressed in the IVS in *Tbx5*$^{CreERT2/flox}$ mutants (*Tbx5*$^{CreERT2/flox}$;*Mef2cAHF-DreERT2*;*ROSA26*$^{Ai6/Ai66}$) with a membranous VSD at E14.5. *Tnnt2* is expressed in cardiomyocytes.(M-X') Expression of *Bmp2*, *Robo1* and *Unc5b* are expressed in the atrioventricular canal (boxed region) in *Tbx5*$^{CreERT2/+}$ controls, and expression of these genes are reduced in *Tbx5*$^{CreERT2/flox}$ mutants.

Figure S7

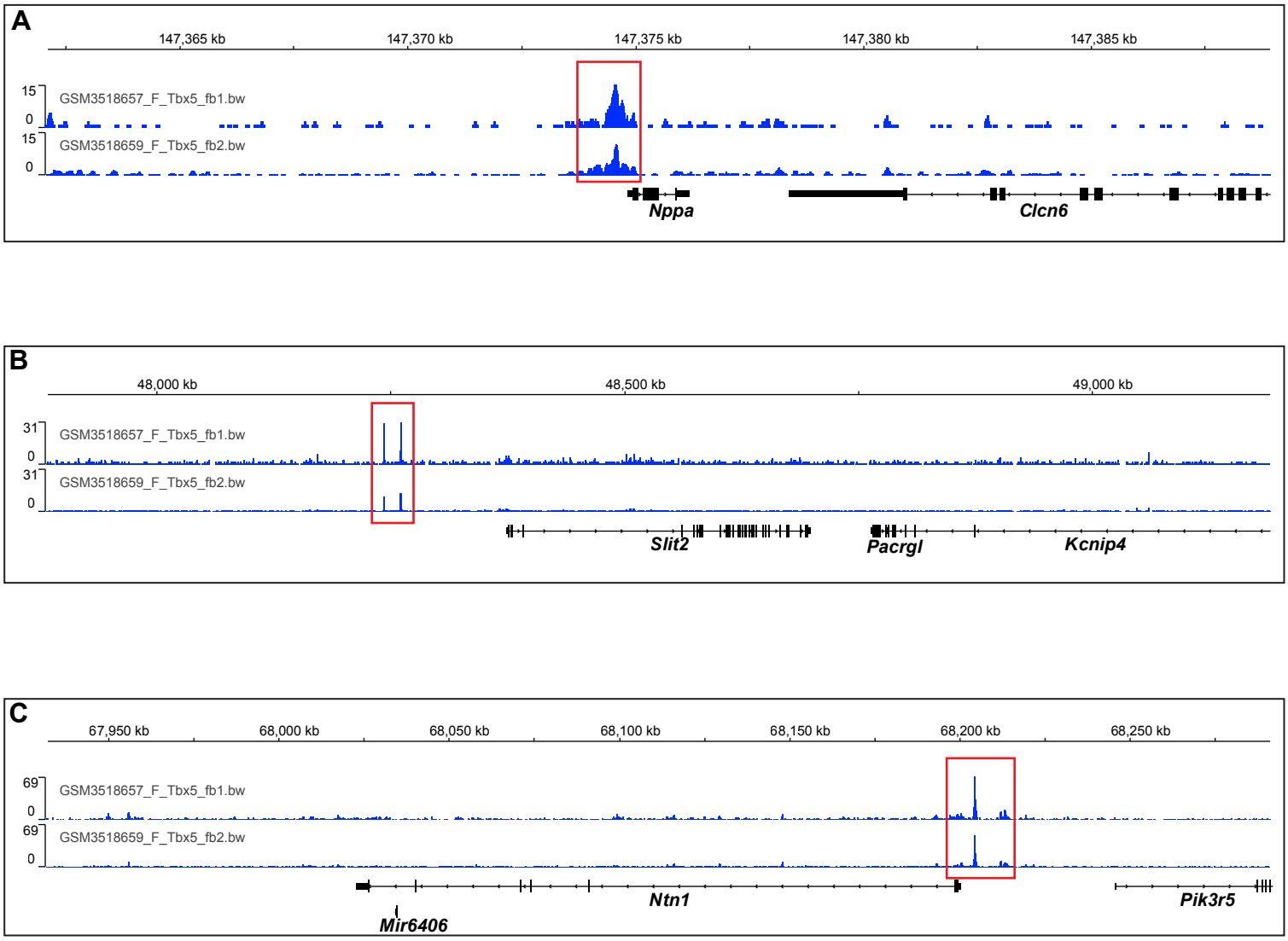

Supplemental Figure 7. TBX5 chromatin occupancy near *Slit2* and *Ntn1*. (A-C) Browser tracks of TBX5 ChIP-seq from E12.5 hearts (from Akerberg et al., 2019) shows peaks of TBX5 occupancy (boxed in red) near promoters of *Nppa*, *Slit2* and *Ntn1*.

Figure S8

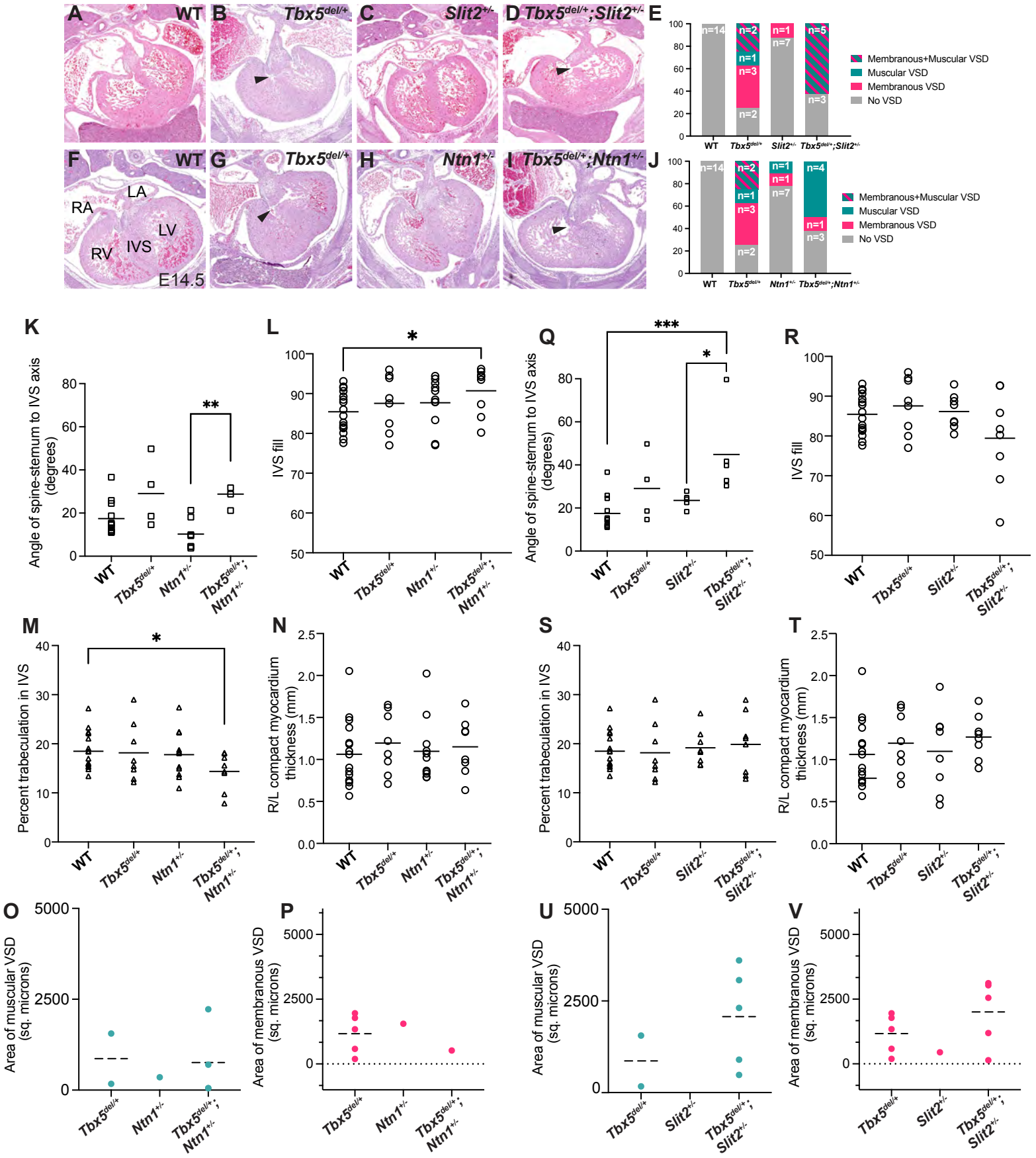

Supplemental Figure 8. *Tbx5-Slit2* and *Tbx5-Ntn1* genetic interactions. Histology from E14.5 embryos from matings of (A-D) *Tbx5*$^{del/+}$ and *Slit2*$^{+/-}$ or (F-I) *Tbx5*$^{del/+}$ and *Ntn1*$^{+/-}$ by genotype. Arrowheads depict muscular ventricular septal defects (VSDs). (E, J) Quantification of membranous or muscular VSDs by genotype. *Tbx5*$^{del/+}$;*Slit2*$^{+/-}$compound heterozygous embryos displayed an estimated decrease in the incidence of membranous VSDs, which approached significance (log OR -2.5; $p<0.09$ in a Generalized Linear Model). *Tbx5*$^{del/+}$;*Ntn1*$^{+/-}$ compound heterozygous embryos displayed a decrease of membranous VSDs (log OR -5.3; $p<1x10^{-3}$ by a Generalized Linear Model), but not changes to prevalence of muscular VSDs (log OR 0.12; $p<0.93$). Machine-learning based quantitative morphometry of metrics for (K-P) *Tbx5*$^{del/+}$ and *Ntn1*$^{+/-}$ or (Q-V) *Tbx5*$^{del/+}$ and *Slit2*$^{+/-}$ by genotype. IVS, interventricular septum. Significance determined by Fisher's exact test (*$p<0.05$, **$p<0.01$, ***$p<0.001$).

Figure 6

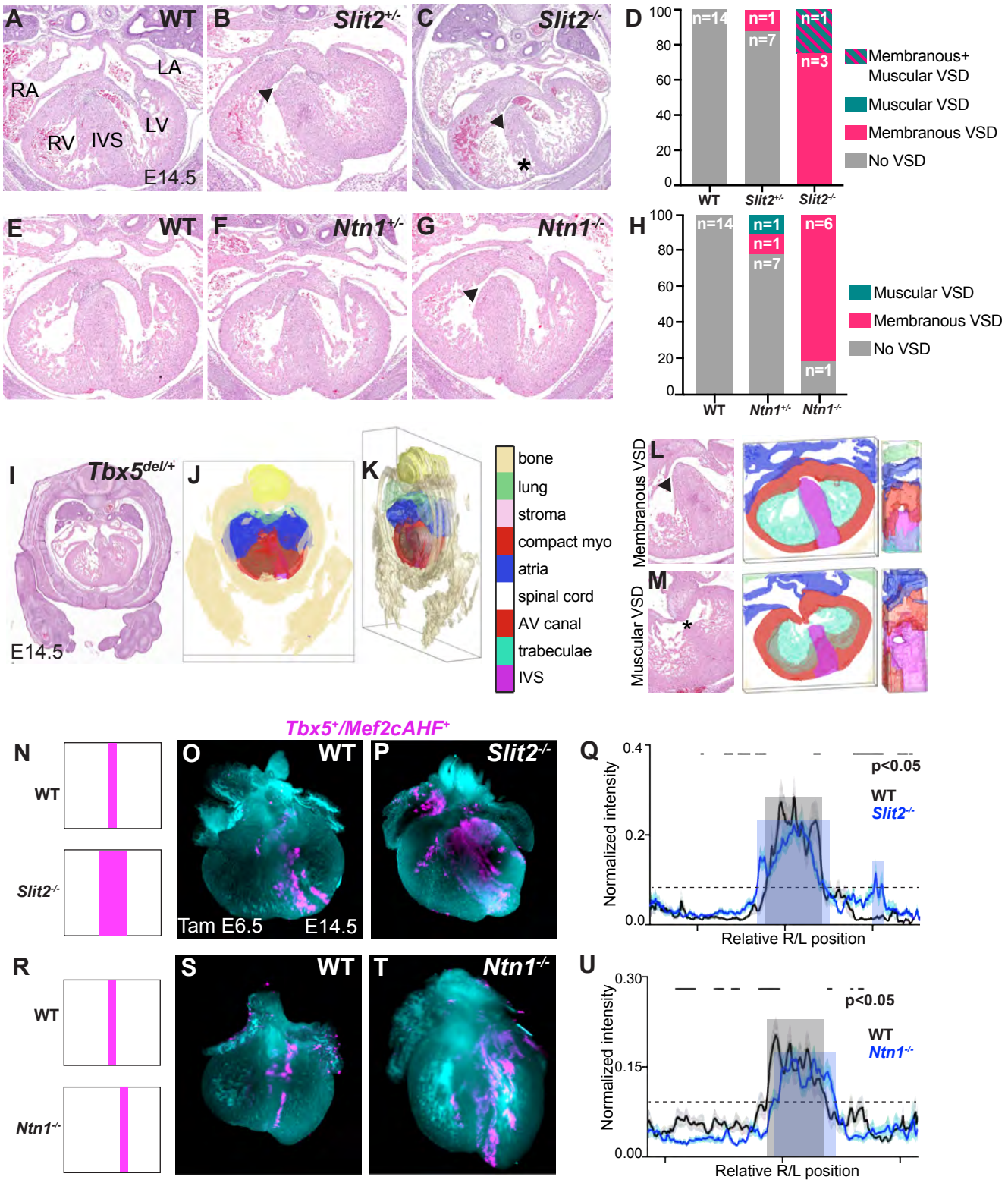

Figure 6. *Slit2* and *Ntn1* are essential for proper ventricular septation and compartment boundary regulation. (A-C) Histology and (D) incidence of muscular or membranous (arrowhead) ventricular septal defects (VSDs) of *Slit2* mutants are shown. Asterisk demarcates non-compacted interventricular septum (IVS) (E-G) Histology and (H) incidence of muscular or membranous ventricular septal defects (VSDs) of *Ntn1* mutants are shown. (I-K) Machine learning-based 3-D reconstructions of the embryonic heart and other tissues from histology at E14.5 were used for quantitative morphometric analysis of the embryonic heart (Supplemental Figure 7, Supplemental Figure 8). Compact myo, compact myocardium; AV canal, atrioventricular canal; IVS, interventricular septum. (L,M) A 3-D reconstruction of a membranous ventricular septal defect (VSD) anteriorly and muscular VSD posteriorly from a *Tbx5*$^{del/+}$ mutant heart. (N-P) Lightsheet imaging of *Slit2*$^{-/-}$ mutant (*Tbx5*$^{CreERT2/+}$;*Mef2cAHF-DreERT2*;*ROSA26*$^{Ai66/+}$;*Slit2*$^{-/-}$)(n=4) hearts at E14.5 showed a broadened distribution of the *Tbx5*$^{+}$/*Mef2cAHF*$^{+}$ lineage (tdTomato^{+} immunostaining) compared to controls (*Tbx5*$^{CreERT2/+}$;*Mef2cAHF-DreERT2*;*ROSA26*$^{Ai66/+}$;*Slit2*$^{+/+}$)(n=2), as (Q) quantified by linear profiles of fluorescence signals above a threshold (dashed line). Gray shading represents control signal above threshold, and periwinkle represents mutant signal. Significance of $p<0.05$ was determined by Welch's two-sample t-test at each position along the right-left axis. (R-T) Lightsheet imaging of *Ntn1*$^{-/-}$ mutant (*Tbx5*$^{CreERT2/+}$;*Mef2cAHF-DreERT2*;*ROSA26*$^{Ai66/+}$;*Ntn1*$^{-/-}$)(n=6) hearts at E14.5 showed a leftward shift in positioning of the *Tbx5*$^{+}$/*Mef2cAHF*$^{+}$ lineage compared to controls (*Tbx5*$^{CreERT2/+}$;*Mef2cAHF-DreERT2*;*ROSA26*$^{Ai66/+}$;*Ntn1*$^{+/+}$)(n=4), as (U) quantified by linear profiles.

Figure S9

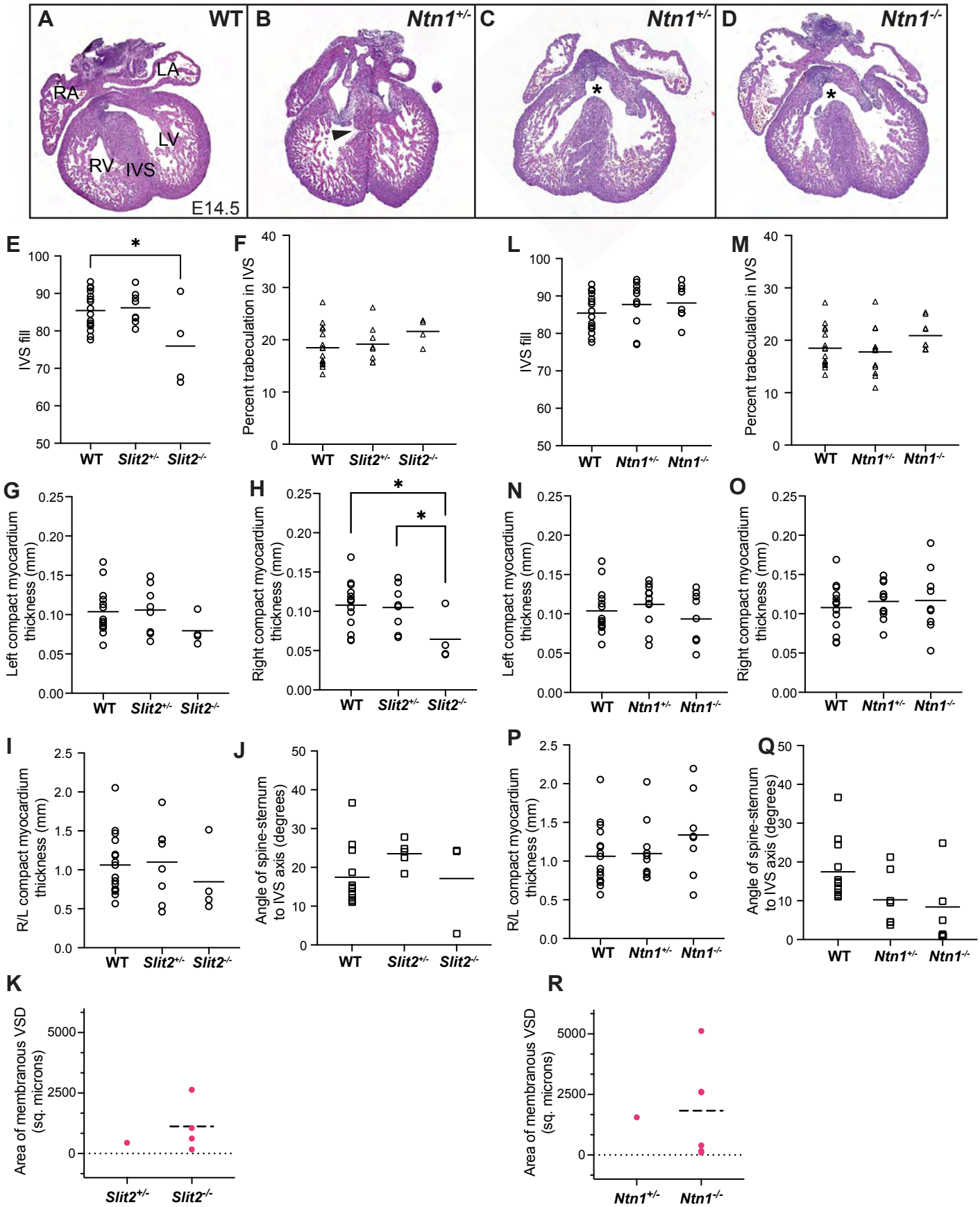

Supplemental Figure 9. Quantitative morphometry of *Slit2* and *Ntn1* mutant hearts. (A-D) Additional histology by *Ntn1* genotype. Arrowhead, muscular ventricular septal defect (VSD). Asterisk, membranous VSD. (E-P) Machine learning-based quantitative cardiac morphometrics for (E-K) *Slit2* or (L-R) *Ntn1* mutants. Significance determined by Fisher's exact test (*$p<0.05$). (Q,R) Morphometry of the area of membranous VSDs by *Slit2* or *Ntn1* genotypes.